Two nucleon systems at $m_\pi \sim 450$ MeV from lattice QCD

Kostas Orginos,[1,2] Assumpta Parreño,[3] Martin J. Savage,[4] Silas R. Beane,[5]
Emmanuel Chang,[4] and William Detmold[6]
(NPLQCD Collaboration)

[1]*Department of Physics, College of William and Mary, Williamsburg, Virginia 23187-8795, USA*
[2]*Jefferson Laboratory, 12000 Jefferson Avenue, Newport News, Virginia 23606, USA*
[3]*Departamento d'Estructura i Constituents de la Matèria and Institut de Ciències del Cosmos (ICC), Universitat de Barcelona, Martí Franquès 1, E08028 Barcelona, Spain*
[4]*Institute for Nuclear Theory, University of Washington, Seattle, Washington 98195-1550, USA*
[5]*Department of Physics, University of Washington, Box 351560, Seattle, Washington 98195, USA*
[6]*Center for Theoretical Physics, Massachusetts Institute of Technology, Cambridge, Massachusetts 02139, USA*

(Received 6 October 2015; published 23 December 2015)

Nucleon-nucleon systems are studied with lattice quantum chromodynamics at a pion mass of $m_\pi \sim 450$ MeV in three spatial volumes using $n_f = 2 + 1$ flavors of light quarks. At the quark masses employed in this work, the deuteron binding energy is calculated to be $B_d = 14.4^{+3.2}_{-2.6}$ MeV, while the dineutron is bound by $B_{nn} = 12.5^{+3.0}_{-5.0}$ MeV. Over the range of energies that are studied, the S-wave scattering phase shifts calculated in the ${}^1S_0$ and ${}^3S_1 - {}^3D_1$ channels are found to be similar to those in nature, and indicate repulsive short-range components of the interactions, consistent with phenomenological nucleon-nucleon interactions. In both channels, the phase shifts are determined at three energies that lie within the radius of convergence of the expansion, allowing for constraints to be placed on the inverse scattering lengths and effective ranges. The extracted phase shifts allow for matching to nuclear effective field theories, from which low-energy counterterms are extracted and issues of convergence are investigated. As part of the analysis, a detailed investigation of the single hadron sector is performed, enabling a precise determination of the violation of the Gell-Mann–Okubo mass relation.

DOI: 10.1103/PhysRevD.92.114512 PACS numbers: 11.15.Ha, 12.38.Gc

I. INTRODUCTION

Calculating the interactions between nucleons and the properties of multinucleon systems directly from quantum chromodynamics (QCD) will be an important milestone in the development of nuclear physics. While lattice QCD (LQCD) calculations of simple hadronic systems are now being performed at the physical light-quark masses and the effects of quantum electrodynamics (QED) are beginning to be included (see, e.g. Ref. [1]), such calculations have not yet been presented for more complex systems such as nuclei. However, remarkable progress has been made in the ongoing efforts to calculate the lowest-lying energy levels of the simplest nuclei and hypernuclei (with $A \leq 4$) and the nucleon-nucleon scattering S-matrix elements [2–22]. The magnetic moments and polarizabilities of the light nuclei have recently been calculated [23,24], and by determining the short-range interaction between nucleons and the electromagnetic field, the first LQCD calculation of the radiative capture process $np \to d\gamma$ [25] was recently performed and the experimentally measured cross section was recovered within the uncertainties of the calculation after extrapolation to the physical quark masses. These calculations represent crucial steps toward verifying LQCD as a useful technique with which to calculate the properties of nuclear systems. However, it will take significant computational resources to reduce the associated uncertainties below those of experiment. Near term advances in the field will come from calculations of quantities that are challenging or impossible to access experimentally, such as multinucleon forces, hyperon-nucleon interactions, rare weak matrix elements and exotic nuclei, such as hypernuclei and charmed nuclei, that are of modest computational complexity. Furthermore, performing calculations specifically to match LQCD results to low-energy effective field theories (EFTs) will provide a means to make first predictions at the physical quark masses and to make predictions of quantities beyond those calculated with LQCD. Such calculations are now under way, using the results of our previous works and those of Yamazaki *et al.*, with the first efforts described, for example, in Ref. [26] for hyperon-nucleon interactions and Ref. [27,28] for nucleon-nucleon interactions and light nuclei.

In this work, we present the results of LQCD calculations of two nucleon systems performed at a pion mass of $m_\pi \sim 450$ MeV in three lattice volumes of spatial extent

TABLE I. Parameters of the ensembles of gauge-field configurations and of the measurements used in this work. The lattices have dimension $L^3 \times T$, a lattice spacing b and a bare quark mass bm_q (in lattice units). $N_{\rm src}$ light-quark sources are used (as described in the text) to perform measurements on $N_{\rm cfg}$ configurations in each ensemble.

Label	L/b	T/b	β	bm_l	bm_s	b [fm]	L [fm]	T [fm]	$m_\pi L$	$m_\pi T$	$N_{\rm cfg}$	$N_{\rm src}$
A	24	64	6.1	−0.2800	−0.2450	0.1167(16)	2.801(29)	7.469(77)	6.390	17.04	4407	1.16×10^6
B	32	96	6.1	−0.2800	−0.2450	0.1167(16)	3.734(38)	11.20(12)	8.514	25.54	4142	3.95×10^5
C	48	96	6.1	−0.2800	−0.2450	0.1167(16)	5.602(58)	11.20(12)	12.78	25.49	1047	6.8×10^4

$L = 2.8$ fm, 3.7 fm and 5.6 fm at a lattice spacing of $b \sim 0.12$ fm. As only one lattice spacing has been employed, extrapolations of the results to the continuum limit have not been performed, although the uncertainties that we finally present encompass the expected effects of these extrapolations. In Sec. II, we introduce the LQCD methods that are used to determine correlation functions and Sec. III reports the results of precision studies of the single hadron systems. Section IV explores the ${}^3S_1 - {}^3D_1$ coupled-channel systems in detail, while the ${}^1S_0$ channel is discussed in Sec. V. In Sec. VI, these channels are further investigated in the context of nucleon-nucleon effective field theory (NNEFT) before the conclusions of the study are presented in Sec. VII.

II. METHODOLOGY

A. Calculational details

LQCD calculations were performed on three ensembles of $n_f = 2 + 1$ isotropic gauge-field configurations with $L = 24$, 32 and 48 lattice sites in each spatial direction, $T = 64$, 96, 96 sites in the temporal direction, respectively, and with a lattice spacing of $b = 0.1167(16)$ fm [29]. The Lüscher-Weisz gauge action [30] was used with a clover-improved quark action [31] with one level of stout smearing ($\rho = 0.125$) [32]. The clover coefficient was set equal to its tree-level tadpole-improved value, a value that is consistent with an independent numerical study of the nonperturbative $c_{\rm SW}$ in the Schrödinger functional scheme [33–35], reducing discretization errors from $\mathcal{O}(b)$ to $\mathcal{O}(b^2)$. The $L = 24$, 32 and 48 ensembles consist of 3.4×10^4, 2.2×10^4 and 1.5×10^4 hybrid Monte Carlo evolution trajectories, respectively. Calculations were performed on gauge-field configurations taken at uniform intervals from these trajectories, see Table I. The strange-quark mass was tuned to that of the physical strange quark, while the selected light-quark mass gave rise to a pion of mass $m_\pi = 449.9(0.3)(0.3)(4.6)$ MeV and a kaon of mass $m_K = 595.9(0.2)(0.2)(6.1)$ MeV. Many details of the current study mirror those of our previous work at the SU(3) symmetric point, which can be found in Refs. [14,17]. In each run on a given configuration, 48 quark propagators were generated from uniformly distributed Gaussian-smeared sources on a cubic grid with an origin randomly selected within the volume. The parameters of the Gaussian smearing are the same as those used in Refs. [14,17]. Multiple runs were performed to increase statistical precision and the total number of measurements is recorded in Table I. Specifics of the ensembles and the number of sources used in each ensemble can also be found in Table I. Quark propagators were computed using the multigrid algorithm [36] or using graphics processing units [37,38] with a tolerance of 10^{-12} in double precision. In the measurements performed on the $L = 24$ and 32 ensembles, the quark propagators, either unsmeared or smeared at the sink using the same parameters as used at the source, provided two sets of correlation functions for each combination of source and sink interpolating fields, labeled as SP and SS, respectively. In contrast, for the measurements performed on the $L = 48$ ensemble only SP correlation functions were produced. The propagators were contracted into baryon blocks that were projected to a well-defined momentum at the sink, that were then used to form the one and two nucleon correlation functions.[1] The blocks are of the form

$$\mathcal{B}_N^{ijk}(\mathbf{p}, t; x_0) = \sum_{\mathbf{x}} e^{i\mathbf{p}\cdot\mathbf{x}} S_i^{(f_1),i'}(\mathbf{x}, t; x_0) S_j^{(f_2),j'}(\mathbf{x}, t; x_0) \times S_k^{(f_3),k'}(\mathbf{x}, t; x_0) b_{i'j'k'}^{(N)}, \quad (1)$$

where $S^{(f)}$ is a quark propagator of flavor $f = u$, d, and the indices are combined spin-color indices running over $i = 1, \ldots, N_c N_s$, where $N_c = 3$ is the number of colors and $N_s = 4$ is the number of spin components. The choice of the f_i and the tensor $b^{(N)}$ depend on the spin and flavor of the nucleon under consideration, and the local interpolating fields constructed in Ref. [39], restricted to those that contain only upper-spin components (in the Dirac spinor basis) are used. This choice results in the simplest interpolating fields that also have good overlap with the nucleon ground states (from localized sources). Blocks are constructed for all lattice momenta $|\mathbf{p}|^2 < 5$ allowing for the study of two nucleon systems with zero or nonzero total momentum. In the production on the $L = 32$ ensemble,

[1] As such, the same Gaussian-smeared quark propagators were used to generate the single-nucleon and two nucleon correlation functions. We have employed a small number of different source and sink structures, as described in Ref. [39], and have presented optimal combinations for each hadron. The ground-state energies extracted from the correlation functions for a given species of hadron are consistent within uncertainties.

correlation functions were produced for all of the spin states associated with each nuclear species. However, only one spin state per species was calculated on the $L = 24$ and $L = 48$ ensembles.

B. Robust estimators: The mean with jacknife and the Hodges-Lehmann estimator with bootstrap

The correlation functions are estimated from calculations performed from many source locations on many gauge-field configurations. On any given configuration, these results are correlated and, because they become translationally invariant after averaging, they can be blocked together to generate one representative correlation function for each configuration. More generally, because of the correlation between nearby configurations produced in a Markov chain, the results obtained over multiple gauge-field configurations are blocked together to produce one representative correlation function from any particular subsequence of the Markov chain. In this work, there are a large number of independent representative correlation functions which, by the central limit theorem, tend to possess a Gaussian-distributed mean. As computational resources are finite, only a finite number of calculations of each correlation function can be performed. The underlying distributions of the nuclear correlation functions are non-Gaussian with extended tails, and therefore outliers are typically present in any sample which lead to slow convergence of the mean. This can then lead to significant fluctuations in estimates of correlation functions when resampling methods, such as bootstrap and jackknife, are employed using the mean to estimate average values (for a discussion of the "noise" associated with these and other such calculations, see Refs. [40–42]). Dealing with outliers of distributions is required in many areas beyond LQCD, and there is extensive literature on *robust estimators* that are resilient to the presence of outliers, such as the median or the Hodges-Lehmann (HL) estimator [43]. The vacuum expectation values of interest in quantum field theory are defined by the mean value of a (generally non-Gaussian) distribution. Nevertheless, with sufficient blocking, the mean of the distribution will be Gaussian distributed, for which the mean, median, mode and HL estimator coincide. It therefore makes sense to consider such robust estimators for large sets of blocked LQCD correlation functions.

While the median of a sample $\{x_i\}$ is well known, the HL estimator is less so. It is a robust and unbiased estimator of the median of a sample, and is defined as [43]

$$\mathrm{HL}(\{x_i\}) = \mathrm{Median}[\{(x_i + x_j)/2\}], \tag{2}$$

where the sample is summed over all $1 < i, j < N$, where N is the sample size. The uncertainty associated with the HL estimator is derived from the median absolute deviation (MAD), defined as

$$\mathrm{MAD}(\{x_i\}) = \mathrm{Median}[\{|x_i - \mathrm{Median}[\{x_i\}]|\}]. \tag{3}$$

For a Gaussian-distributed sample, $1\sigma = 1.4826$ MADs. The median, HL estimator and other similar estimators cannot be computed straightforwardly under jackknife, and instead such analyses are performed with bootstrap resampling.

In the present work, the correlation functions, and their ratios, are analyzed using both the mean under jackknife and HL under bootstrap, from ~100 representative correlation functions constructed by blocking the full set of correlation functions. In almost all cases, the HL with bootstrap gives rise to smaller statistical fluctuations over the resampled ensembles and, consequently, to smaller uncertainties in estimates of energies, as seen in our previous investigation into robust estimators [44]. It is found that outlying blocked correlation functions cause a significant enlargement of the estimated variance of the mean, while the robust HL estimator is insensitive to them.

III. SINGLE MESONS AND BARYONS

Precision measurements of the single hadron masses, their dispersion relations and their volume dependence are essential for a complete analysis of multinucleon systems, in particular for a complete quantification of the uncertainties in binding energies and S-matrix elements. Single hadron correlation functions for the $\pi^{\pm}$, $\rho^{\pm}$, $K^{\pm}$, $K^{*,\pm}$, the octet baryons and the decuplet baryons were calculated in each of the three lattice volumes at six different momenta (in each volume), from which ground-state energies for each momentum were extracted. The hadron energies were extracted from plateaus in the effective mass plots (EMPs) derived from linear combinations (in the $L = 24$ and 32 ensembles) of the SP and SS correlation functions calculated at each lattice momentum. The EMPs associated with the $\pi^{\pm}$ and $K^{\pm}$ are shown in Figs. 1 and 2, respectively, while the EMPs for the octet baryons are shown in Figs. 3, 4, 5 and 6.

It is clear from the EMPs that extended ground-state plateaus exists for all hadrons at all momenta, and as such relatively precise hadron masses and dispersion relations can be determined. As only SP correlation functions were calculated for the $L = 48$ ensemble, the ground-state plateaus set in at larger times for each hadron in this ensemble than in the $L = 24$ or $L = 32$ ensembles. A correlated χ^2-minimization fit of the plateau region in combinations of correlation function to a constant energy was performed over a range of fit intervals to determine the energy, its statistical uncertainty and the systematic uncertainty due to the selection of the fitting range. The energies of the pseudoscalar mesons and octet baryons are shown in Tables II and III, respectively.

The energies determined at zero momentum are used to extrapolate the hadron masses to infinite volume, and

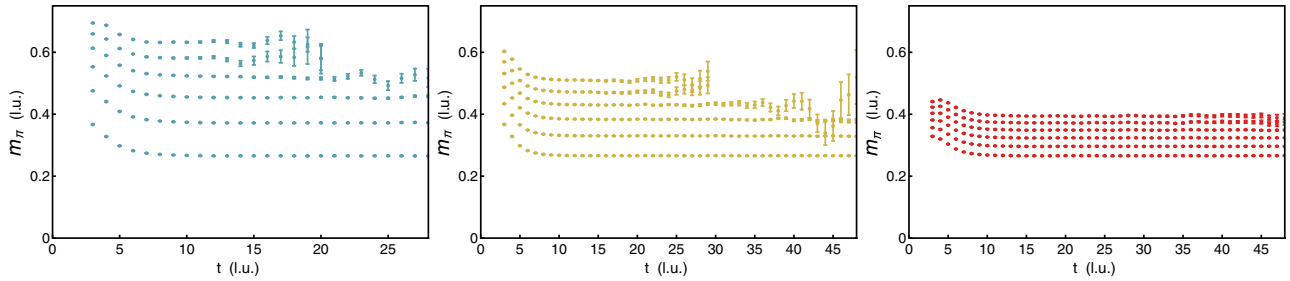

FIG. 1 (color online). Cosh EMPs for the $\pi^{\pm}$ in the $L = 24$ (left panel), $L = 32$ (center panel), $L = 48$ (right panel) lattice volumes, respectively. In ascending order, the momenta are $\mathbf{P} = 2\pi\mathbf{n}/L$ with $|\mathbf{n}|^2 = 0, 1, 2, 3, 4, 5$.

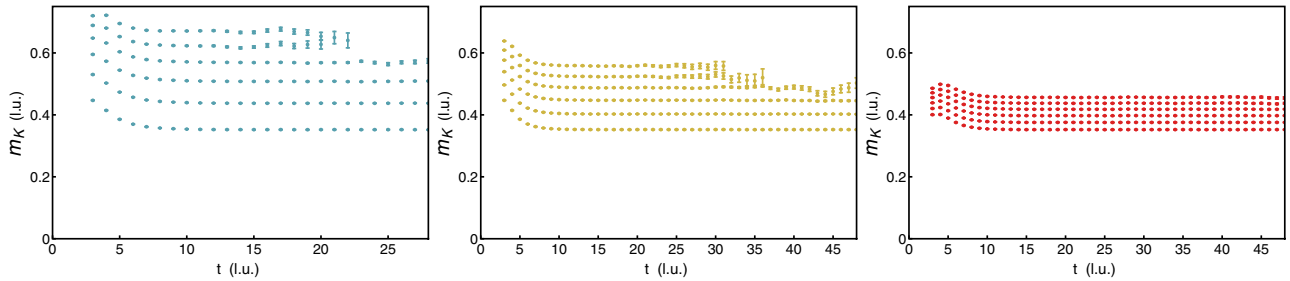

FIG. 2 (color online). Cosh EMPs for the $K^{\pm}$ in the $L = 24$ (left panel), $L = 32$ (center panel), $L = 48$ (right panel) lattice volumes, respectively. In ascending order, the momenta are $\mathbf{P} = 2\pi\mathbf{n}/L$ with $|\mathbf{n}|^2 = 0, 1, 2, 3, 4, 5$.

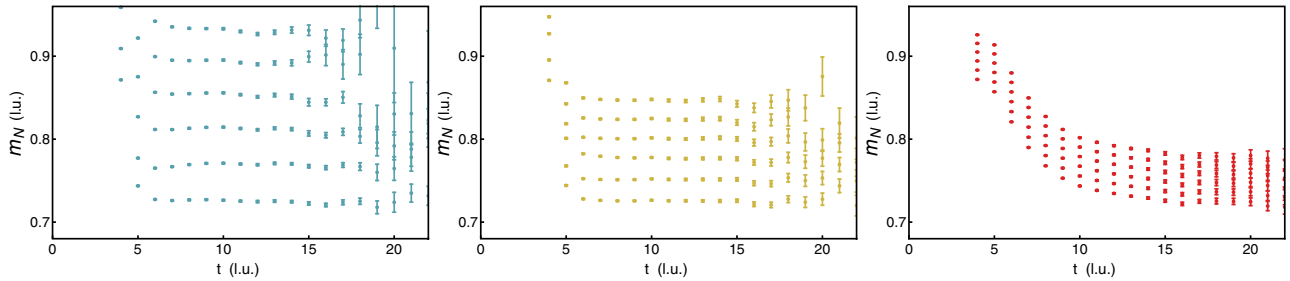

FIG. 3 (color online). EMPs for the nucleon in the $L = 24$ (left panel), $L = 32$ (center panel), $L = 48$ (right panel) lattice volumes, respectively. In ascending order, the momenta are $\mathbf{P} = 2\pi\mathbf{n}/L$ with $|\mathbf{n}|^2 = 0, 1, 2, 3, 4, 5$.

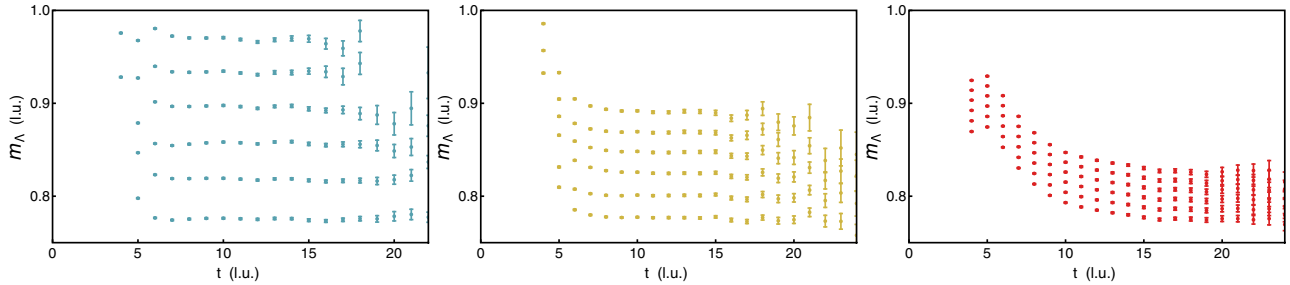

FIG. 4 (color online). EMPs for the Λ in the $L = 24$ (left panel), $L = 32$ (center panel), $L = 48$ (right panel) lattice volumes, respectively. In ascending order, the momenta are $\mathbf{P} = 2\pi\mathbf{n}/L$ with $|\mathbf{n}|^2 = 0, 1, 2, 3, 4, 5$.

are combined with the other energies to determine their dispersion relations. With the large values of $m_\pi L$ in the ensembles of gauge configurations, it is sufficient to use the leading-order (LO) finite-volume (FV) corrections to the hadron masses to extrapolate from the volumes of the calculations to infinite volume. The LO modifications to the pseudoscalar masses, m_M, and baryon masses, M_B, are given by

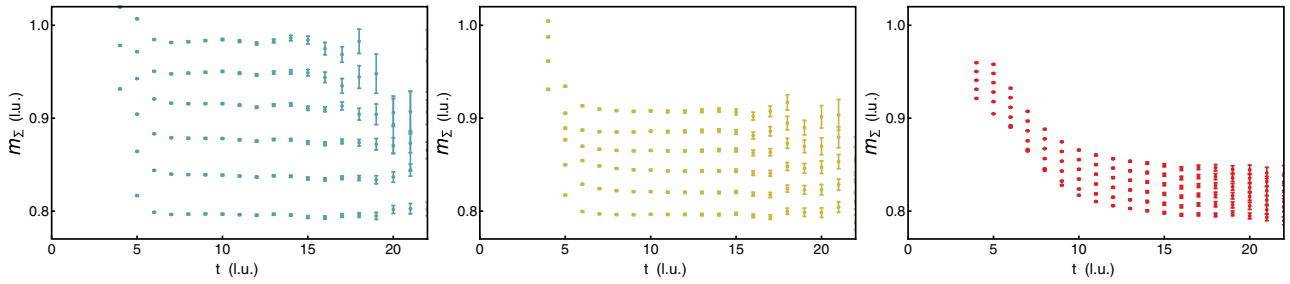

FIG. 5 (color online). EMPs for the Σ in the $L = 24$ (left panel), $L = 32$ (center panel), $L = 48$ (right panel) lattice volumes, respectively. In ascending order, the momenta are $\mathbf{P} = 2\pi\mathbf{n}/L$ with $|\mathbf{n}|^2 = 0$, 1, 2, 3, 4, 5.

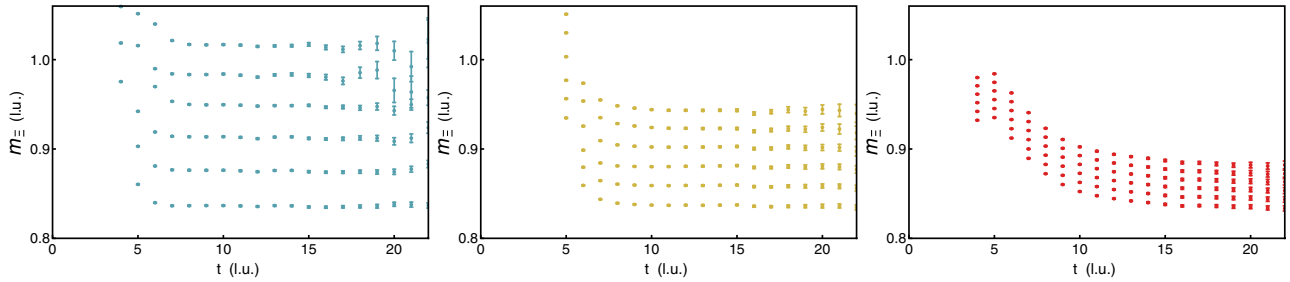

FIG. 6 (color online). EMPs for the Ξ in the $L = 24$ (left panel), $L = 32$ (center panel), $L = 48$ (right panel) lattice volumes, respectively. In ascending order, the momenta are $\mathbf{P} = 2\pi\mathbf{n}/L$ with $|\mathbf{n}|^2 = 0$, 1, 2, 3, 4, 5.

$$m_M^{(V)}(m_\pi L) = m_M^{(\infty)} + c_M \frac{e^{-m_\pi L}}{(m_\pi L)^{3/2}} + \cdots$$
$$M_B^{(V)}(m_\pi L) = M_B^{(\infty)} + c_B \frac{e^{-m_\pi L}}{m_\pi L} + \cdots, \qquad (4)$$

where the forms are those of p-regime chiral perturbation theory (χPT) and heavy-baryon χPT [45]. The infinite-volume masses, $m_M^{(\infty)}$ and $M_B^{(\infty)}$, and the coefficients of the LO volume dependence, c_M and c_B, are quantities determined by fits to the LQCD calculations, and will, in general, be different for each hadron.

The zero-momentum energies of the pseudoscalar mesons and their infinite-volume extrapolation are given in Table II and shown in Fig. 7. The energies of both mesons are found to be independent of the lattice volume within the uncertainties of the calculations. Despite the larger number of correlation functions in the $L = 24$ ensemble, the uncertainties in the meson masses are larger than those extracted from the $L = 32$ ensemble. The zero-momentum energies of the octet baryons and their infinite-volume extrapolation are given in Table III and shown in Fig. 8. As with the mesons, there is no statistically significant volume dependence observed for any of the octet-baryon masses. Two-parameter χ^2-minimization fits of the form given in Eq. (4) were performed to the volume dependence of each hadron to extract its infinite-volume mass. Because of the negligible volume dependence in the LQCD results, limited

TABLE II. The pion and kaon energies (l.u.) as a function of momentum (l.u.), $|\mathbf{P}| = (\frac{2\pi}{L})|\mathbf{n}|$, calculated on each ensemble of gauge-field configurations. The infinite-volume meson masses, determined by fitting expressions of the form in Eq. (4), are also given. The first uncertainty associated with each extraction is statistical and the second is the fitting systematic. In the case of the extrapolated values, the systematic uncertainty also contains the estimated uncertainty due to the extrapolation (which is small in both cases).

Meson	Ensemble	$\lvert\mathbf{n}\rvert = 0$	$\lvert\mathbf{n}\rvert^2 = 1$	$\lvert\mathbf{n}\rvert^2 = 2$	$\lvert\mathbf{n}\rvert^2 = 3$	$\lvert\mathbf{n}\rvert^2 = 4$	$\lvert\mathbf{n}\rvert^2 = 5$
$\pi^\pm$	$24^3 \times 64$	0.26626(36)(14)	0.37184(28)(34)	0.45341(30)(45)	0.5204(07)(13)	0.5812(10)(17)	0.6329(09)(12)
	$32^3 \times 96$	0.26607(23)(09)	0.33006(20)(14)	0.38330(21)(16)	0.43042(26)(28)	0.47156(43)(93)	0.5093(05)(12)
	$48^3 \times 96$	0.26607(17)(11)	0.29624(14)(05)	0.32365(13)(10)	0.34895(16)(10)	0.37221(22)(18)	0.39404(31)(35)
	$L = \infty$	0.26606(14)(08)					
$K^\pm$	$24^3 \times 64$	0.35239(30)(16)	0.43749(24)(25)	0.50810(22)(25)	0.56947(35)(50)	0.6224(07)(13)	0.67109(52)(55)
	$32^3 \times 96$	0.35248(18)(08)	0.40259(16)(17)	0.44725(17)(09)	0.48782(24)(49)	0.52357(45)(60)	0.55727(46)(88)
	$48^3 \times 96$	0.35236(16)(25)	0.37559(13)(06)	0.39744(13)(06)	0.41814(13)(06)	0.43760(17)(05)	0.45628(21)(09)
	$L = \infty$	0.35240(11)(03)					

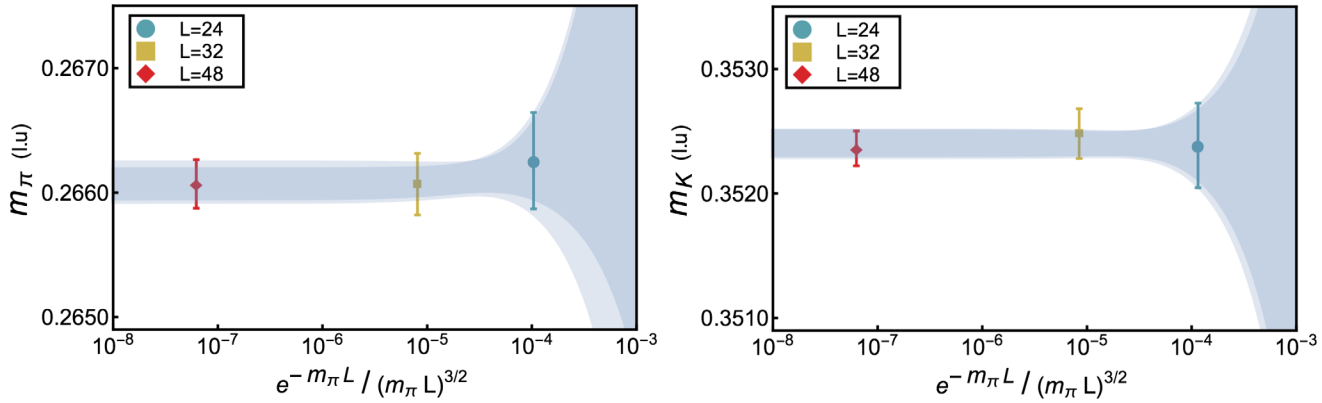

FIG. 7 (color online). The volume dependence of the π^+ (left panel) and $K^\pm$ (right panel) masses. Energies (l.u.) in the $L = 24$, 32 and 48 lattice volumes are shown as the blue, yellow and red points, respectively, while the results of fits to these results of the form given in Eq. (4) are shown by the shaded regions with the inner (outer) band denoting the statistical (statistical and systematic combined in quadrature) uncertainties.

constraints can be placed on the $c_{M,B}$ coefficients. In addition to the $\pi^\pm$, $K^\pm$ and octet baryons, analogous extrapolations were performed with the results obtained for the $\rho^\pm$, $K^{*\pm}$ and decuplet baryons, the combined results of which are shown in Table IV (in both l.u. and MeV).

Deviations of the single hadron dispersion relations from that of special relativity lead to modifications to Lüscher's quantization conditions (QCs) in two-body systems. To address this, the dispersion relations have been precisely determined, and the deviations from special relativity are propagated through the extraction of S-matrix elements using the QCs. In each of the ensembles, single hadron correlation functions were calculated for each of the hadrons of interest with momenta $|\mathbf{p}| \leq \sqrt{5}(2\pi/L)$, the results of which are given in Tables II and III. Energy-momentum relations that are fit to the results obtained for each hadron, h, are of the form

$$E_h^2 = M_h^2 + v_h^2|\mathbf{p}|^2 + \eta_h(|\mathbf{p}|^2)^2, \tag{5}$$

where the hadron speed of light, v_h, and the higher-order deviation from special relativity, parametrized by η_h, are determined by fits to the results of the LQCD calculations. With this parametrization, the v_h's are consistent with unity

TABLE III. The baryon energies (l.u.) as a function of momentum (l.u.), $|\mathbf{P}| = (\frac{2\pi}{L})|\mathbf{n}|$, calculated on each ensemble of gauge-field configurations. The infinite-volume masses, determined by fitting the expression in Eq. (4), are also given. The first uncertainty is statistical and the second is the fitting systematic. In the case of the extrapolated values, the systematic uncertainty also contains the estimated uncertainty due to the extrapolation (which is small in all cases).

Baryon	Ensemble	$\|\mathbf{n}\| = 0$	$\|\mathbf{n}\|^2 = 1$	$\|\mathbf{n}\|^2 = 2$	$\|\mathbf{n}\|^2 = 3$	$\|\mathbf{n}\|^2 = 4$	$\|\mathbf{n}\|^2 = 5$
	$24^3 \times 64$	0.7251(04)(11)	0.7699(10(13)	0.8108(10)(13)	0.8497(13)(21)	0.8944(16)(23)	0.9311(17)(23)
N	$32^3 \times 96$	0.72546(47)(31)	0.75160(60)(47)	0.77657(75)(89)	0.80098(62)(81)	0.8238(07)(11)	0.8467(07)(10)
	$48^3 \times 96$	0.7245(10)(13)	0.7359(21)(34)	0.7471(23)(35)	0.7556(20)(36)	0.7661(21)(40)	0.7771(22)(42)
	$L = \infty$	0.72524(46)(35)					
	$24^3 \times 64$	0.77609(42)(66)	0.8165(14)(18)	0.8533(14)(21)	0.8918(23)(34)	0.9336(14)(22)	0.9709(12)(16)
Λ	$32^3 \times 96$	0.77633(45)(48)	0.80059(60)(48)	0.82435(75)(51)	0.84687(78)(54)	0.8680(10(14)	0.8900(08)(10)
	$48^3 \times 96$	0.77650(94)(80)	0.7858(14)(20)	0.7963(14)(21)	0.8066(15)(23)	0.8166(16)(27)	0.8268(16)(29)
	$L = \infty$	0.77638(42)(48)					
	$24^3 \times 64$	0.79520(70)(65)	0.83608(73)(62)	0.87550(75)(87)	0.9147(07)(13)	0.9485(07)(10)	0.9855(10)(24)
Σ	$32^3 \times 96$	0.79634(31)(49)	0.82033(60)(61)	0.84320(63)(75)	0.86502(71)(51)	0.88575(60)(57)	0.90755(65)(63)
	$48^3 \times 96$	0.7958(12)(13)	0.8050(14)(23)	0.8152(15)(24)	0.8253(16)(26)	0.8351(16)(28)	0.8451(17)(30)
	$L = \infty$	0.79638(33)(54)					
	$24^3 \times 64$	0.83646(63)(49)	0.87594(60)(58)	0.91318(58)(54)	0.9487(06)(10)	0.9828(06)(11)	1.01668(60)(95)
Ξ	$32^3 \times 96$	0.83715(53)(58)	0.85886(49)(59)	0.88044(50)(57)	0.90201(51)(36)	0.92261(62)(89)	0.94276(66)(89)
	$48^3 \times 96$	0.83643(68)(72)	0.8460(11)(10)	0.8557(12)(11)	0.8652(12)(13)	0.8744(13)(14)	0.8837(14)(17)
	$L = \infty$	0.83690(45)(50)					

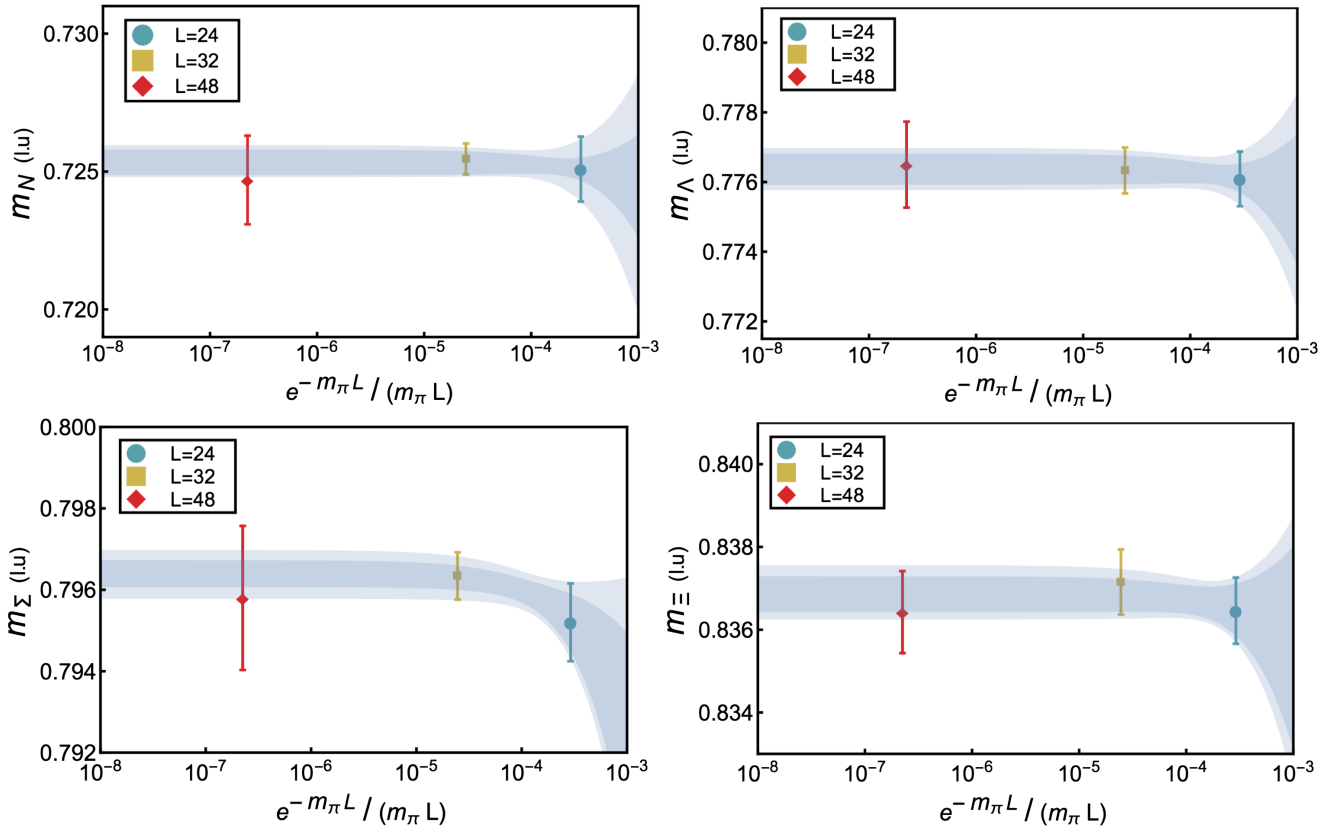

FIG. 8 (color online). The volume dependence of the N, Λ, Σ and Ξ masses. Energies (l.u.) in the $L = 24$, 32 and 48 lattice volumes are shown as the blue, yellow and red points, respectively, while fits to these results are shown by the gray, shaded regions with the inner (outer) band denoting the statistical (statistical and systematic combined in quadrature) uncertainties.

and the η_h's are consistent with zero (for all hadrons). There is a Lorentz-breaking term that could be considered at this order in a momentum expansion, $\sum_j \mathbf{p}_j^4$, but this is also found to be consistent with zero. The energies of the $\pi^\pm$, $K^\pm$ and octet baryons as a function of momentum are given in Tables II and III and shown in Figs. 9 and 10. χ^2-minimization fits to the energy-momentum dispersion relation are performed to extract the speed of light for each hadron, the results of which are shown in Table V. In the low-energy regime relevant to the two nucleon systems, the dispersion relation of special relativity is found to hold at the $\sim$1% level.

A. The Gell-Mann–Okubo mass relation

Given the precise determinations of the single hadron spectrum, it is important to test relations between baryon masses that are predicted to hold in particular limits of QCD. The Gell-Mann–Okubo mass relation [46,47] arises from SU(3) flavor symmetry and its violation, quantified by

$$T_{\rm GMO} = M_\Lambda + \frac{1}{3}M_\Sigma - \frac{2}{3}M_N - \frac{2}{3}M_\Xi, \qquad (6)$$

results from SU(3) breaking transforming in the **27**-plet irreducible representation (irrep) of flavor SU(3) which can

TABLE IV. The infinite-volume hadron masses obtained by extrapolating zero-momentum ground-state energies with the volume dependence given in Eq. (4). The first and second uncertainties are the statistical and systematic, respectively, while the third for values in units of MeV results from the uncertainty in the scale setting.

Hadron	Mass (l.u.)	Mass (MeV)	Hadron	Mass (l.u.)	Mass (MeV)
$\pi^\pm$	0.26614(15)(15)	449.9(0.3)(0.3)(4.6)	$K^\pm$	0.35241(12)(11)	595.9(0.2)(0.2)(6.1)
$\rho^\pm$	0.5248(14)(15)	887.3(2.4)(2.5)(9.1)	$K^{*\pm}$	0.56923(89)(51)	962.4(1.5)(0.9)(9.9)
N	0.72524(46)(35)	1226(01)(01)(12)	Λ	0.77638(42)(48)	1312(01)(01)(13)
Σ	0.79638(33)(54)	1346(01)(01)(14)	Ξ	0.83690(45)(50)	1415(01)(01)(15)
Δ	0.8791(14)(17)	1486(02)(03)(15)	Σ^*	0.9211(17)(19)	1557(03)(03)(16)
Ξ^*	0.9637(09)(17)	1629(02)(03)(17)	Ω	1.0059(06)(12)	1700(01)(02)(17)

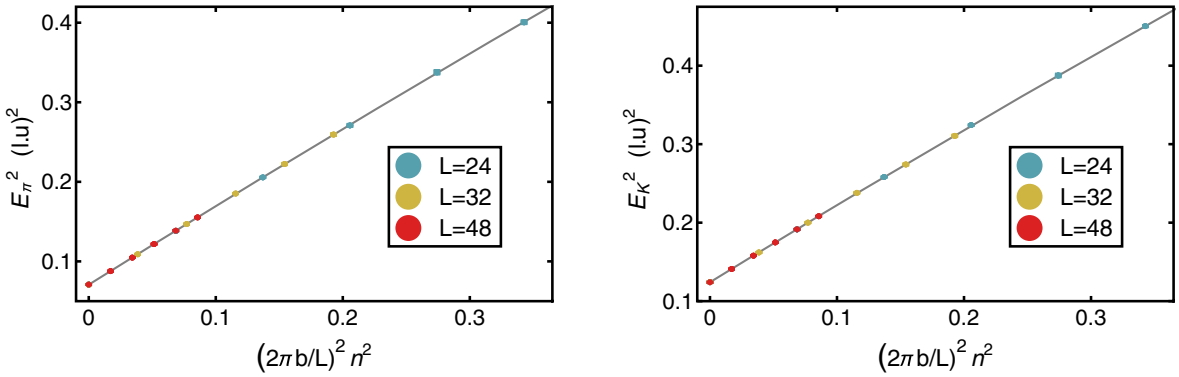

FIG. 9 (color online). Dispersion relations of the $\pi^{\pm}$, $K^{\pm}$. The results in the $L = 24$, 32 and 48 lattice volumes are shown as the blue, yellow and red points, respectively, while fits to these results are shown by the gray curves.

only arise from multiple insertions of the light-quark mass matrix or from nonanalytic meson-mass dependence induced by loops in χPT. Furthermore, it has been shown that $T_{\rm GMO}$ vanishes in the large-N_c limit as $1/N_c$ [48]. In a previous work [49], we performed the first LQCD determination of this quantity, after which more precise LQCD determinations [50] were performed. In this work, by far the most precise determination of $T_{\rm GMO}$ was obtained from the $L = 32$ ensemble, where we find $T_{\rm GMO} = +0.000546(51)(81)$ l.u. $= +0.92(09)(14)(01)$ MeV [compared with $T_{\rm GMO} = +0.00056(19)(38)$l.u.$= +0.96(33)(64)(01)$MeV and $T_{\rm GMO} = +0.00104(27)(29)$ l.u. $= +1.76(46)(49)(02)$ MeV, from the $L = 24$ and 48 ensembles, respectively]. It is conventional to form the dimensionless quantity $\delta_{\rm GMO} = T_{\rm GMO}/M_0$, where M_0 is the centroid of the octet-baryon masses. In the present calculations, the centroid is found to be $M_0 = 0.78658(51)(36)$ l.u. $= 1329(01)(01)(14)$ MeV, from which $\delta_{\rm GMO} = 0.00069(06)(10)$. This value is consistent with our previously published result close to this pion mass and is also consistent with other subsequent determinations [50], but far more precise. However, as the present calculations have been

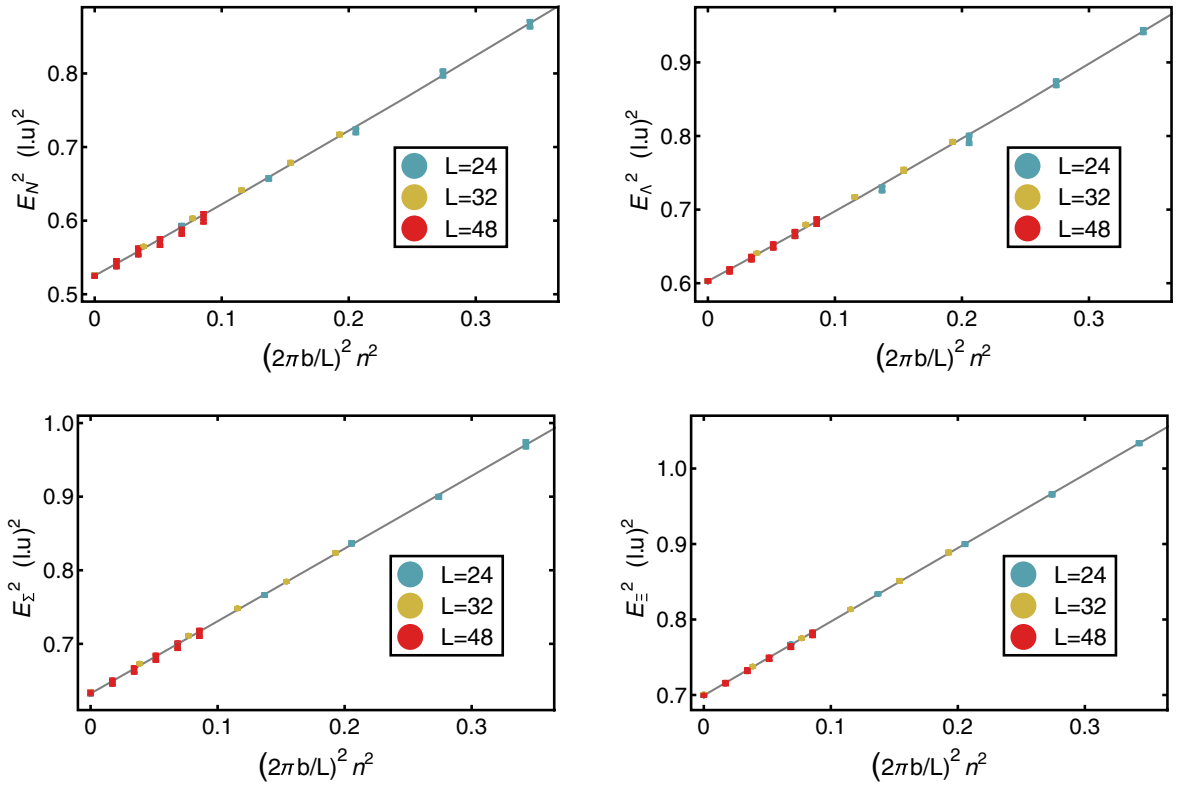

FIG. 10 (color online). Dispersion relations of the octet baryons. The results in the $L = 24$, 32 and 48 lattice volumes are shown as the blue, yellow and red points, respectively, while fits to these results are shown by the gray curves.

TABLE V. The speed of light of each hadron determined from fits to the energy-momentum results.

Hadron	v_h	Hadron	v_h
$\pi^\pm$	1.0025(18)(08)	$K^\pm$	1.0038(20)(12)
N	1.010(16)(07)	Λ	1.018(15)(01)
Σ	1.010(12)(03)	Ξ	1.0102(61)(13)

performed at only one lattice spacing, there is a systematic uncertainty associated with extrapolating to the continuum that is not directly quantified, but which we have estimated to be small. It is worth noting that the experimental value, $T_{\rm GMO}^{\rm expt} = +8.76(08)$ MeV, is an order of magnitude larger than the value we have determined at this heavier pion mass.

IV. THE $^3S_1 - {}^3D_1$ COUPLED CHANNELS AND THE DEUTERON

The phenomenology of the $^3S_1 - {}^3D_1$ coupled $J = 1$ channels in finite volumes has been explored recently using the experimentally constrained phase shifts and mixing angles in an effort to understand what might be expected in future LQCD calculations [51]. One goal of that study was to estimate the lattice volumes and identify the correlation functions required to extract the phase shifts and mixing parameter describing these channels in infinite volume. It was found to be convenient in those FV studies [51] to use the Blatt-Biedenharn [52] parametrization of the 2×2 S-matrix (below the inelastic threshold),

$$S_{(J=1)} = \begin{pmatrix} \cos\epsilon_1 & -\sin\epsilon_1 \\ \sin\epsilon_1 & \cos\epsilon_1 \end{pmatrix} \begin{pmatrix} e^{2i\delta_{1\alpha}} & 0 \\ 0 & e^{2i\delta_{1\beta}} \end{pmatrix} \times \begin{pmatrix} \cos\epsilon_1 & \sin\epsilon_1 \\ -\sin\epsilon_1 & \cos\epsilon_1 \end{pmatrix}, \tag{7}$$

from which the QCs associated with these channels can be determined. For the two nucleon system at rest in a cubic volume, embedded in the even-parity $\mathbb{T}_1$ irrep of the cubic group, the QC in the limit of vanishing $\delta_{1\beta}$, D-waves and higher phase shifts becomes [51]

$$k^*_{\mathbb{T}_1} \cot\delta_{1\alpha}(k^*_{\mathbb{T}_1}) = 4\pi c_{00}^{(0,0,0)}(k^*_{\mathbb{T}_1}; L), \tag{8}$$

where $k^*_{\mathbb{T}_1}$ is the magnitude of the momentum in the center-of-momentum (CoM) frame, and the function $c_{00}^{(0,0,0)}(k^*_{\mathbb{T}_1}; L)$ is proportional to the Lüscher $\mathcal{Z}_{00}$ function, as given in Refs. [53,54]. The phase shift $\delta_{1\alpha}$ is evaluated at $k^*_{\mathbb{T}_1}$. The three j_z substates are degenerate and their energies are insensitive to the mixing parameter ϵ_1.

In contrast, for the two nucleon system carrying one unit of lattice momentum along the z axis, $\mathbf{P}_{\rm tot.} = \frac{2\pi}{L}\mathbf{d}$ with $\mathbf{d} = (0, 0, 1)$, the three substates are embedded into two distinct even-parity irreps of the cubic group—the one-dimensional $\mathbb{A}_2$ representation and the two-dimensional $\mathbb{E}$ representation, containing the $j_z = 0$ and $j_z = \pm 1$ states, respectively. In the same limit as taken to derive Eq. (8), the QCs for these two irreps are [51]

$$\begin{aligned} k^*_{\mathbb{A}_2} \cot\delta_{1\alpha}(k^*_{\mathbb{A}_2}) &= 4\pi c_{00}^{(0,0,1)}(k^*_{\mathbb{A}_2}; L) \\ &\quad - \frac{1}{\sqrt{5}} \frac{4\pi}{k^{*2}_{\mathbb{A}_2}} c_{20}^{(0,0,1)}(k^*_{\mathbb{A}_2}; L) s_{\epsilon_1}(k^*_{\mathbb{A}_2}), \\ k^*_{\mathbb{E}} \cot\delta_{1\alpha}(k^*_{\mathbb{E}}) &= 4\pi c_{00}^{(0,0,1)}(k^*_{\mathbb{E}}; L) \\ &\quad + \frac{1}{2\sqrt{5}} \frac{4\pi}{k^{*2}_{\mathbb{E}}} c_{20}^{(0,0,1)}(k^*_{\mathbb{E}}; L) s_{\epsilon_1}(k^*_{\mathbb{E}}), \end{aligned} \tag{9}$$

where

$$s_{\epsilon_1}(k^*) = \sqrt{2} \sin 2\epsilon_1(k^*) - \sin^2\epsilon_1(k^*). \tag{10}$$

The difference in energy between the $\mathbb{A}_2$ and $\mathbb{E}$ FV eigenstates provides a measure of ϵ_1, but this is complicated by the fact that they are evaluated at two slightly different energies. This analysis can be extended to other lattice momenta [51], but the QCs in Eqs. (8) and (9) are sufficient for the present purposes.

Correlation functions for two nucleons in the $\mathbb{T}_1$, $\mathbb{A}_2$ and $\mathbb{E}$ irreps are straightforwardly constructed from the nucleon blocks we have described previously. In fact, multiple correlation functions are constructed in each irrep. In the $L = 24$ and 48 ensembles, the spin projections were not performed to permit construction of the $\mathbb{A}_2$ irrep, and so only $L = 32$ correlation functions can be used to constrain ϵ_1.

A. The deuteron

In nature, the deuteron is the only bound state in the two nucleon systems, residing in the $^3S_1 - {}^3D_1$ coupled channels, and it has a special position in nuclear physics. The deuteron has always provided a benchmark when deriving phenomenological interactions between nucleons, and it will play a critical role in verifying LQCD as a viable calculational tool. Correlation functions for two nucleons in the even-parity $\mathbb{T}_1$ irrep of the cubic group were constructed, from which, after a correlated subtraction of twice the energy of a single nucleon, the EMPs shown in Fig. 11 were derived.[2] As with the single hadrons,

[2]The single-nucleon correlation function, the square of which is divided out of two nucleon correlation functions to yield a plateau in the energy difference, has been temporally displaced, in some instances, to enhance the plateau region in the difference. Furthermore, due to the nature of the HL estimator, the first few time slices in the difference correlation function have been removed, leading to temporal displacements of the EMPs. The EMPs defining energy differences in this work correspond to both the one nucleon and two nucleon correlation functions being in their respective ground states (as defined by plateaus in their respective individual EMPs).

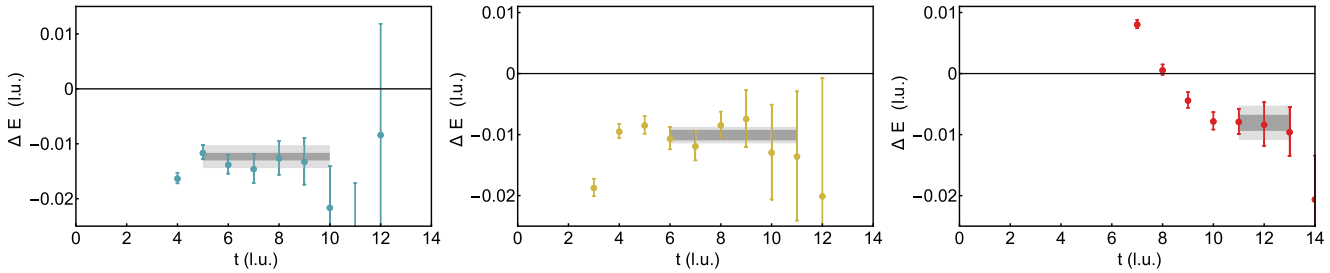

FIG. 11 (color online). EMPs for the energy difference between the deuteron and twice the nucleon in the $L = 24$ (left panel), $L = 32$ (center panel) and $L = 48$ (right panel) ensembles, along with fits to the plateau regions. The extracted binding energies are given in Table VI.

correlated χ^2-minimization fits of a constant to the plateau regions were performed to estimate the deuteron binding energy, B_d, and associated uncertainties. The deuteron binding energies extracted from each ensemble are given in Table VI, along with the values of $e^{-\kappa L}$, where $\kappa = \sqrt{M_N B_d}$ is the binding momentum of the deuteron. As $e^{-\kappa L}$ is seen to change from ∼3% in the largest volume to ∼11% in the smallest, an extrapolation in volume is desirable.

Inspired by the FV contributions to the binding of a shallow bound state resulting from short-range interactions [55–57], the extrapolation to infinite volume was performed by fitting a function of the form

$$B_d(L) = B_d^{(\infty)} + c_1 \left[\frac{e^{-\kappa_0 L}}{L} + \sqrt{2}\frac{e^{-\sqrt{2}\kappa_0 L}}{L} + \frac{4}{3\sqrt{3}}\frac{e^{-\sqrt{3}\kappa_0 L}}{L} \right] + \cdots \tag{11}$$

to the results obtained in the three lattice volumes, where $\kappa_0 = \sqrt{M_N B_d^{(\infty)}}$ (with $B_d^{(\infty)}$ the deuteron binding energy in infinite volume) and c_1 are the fit parameters. The ellipsis denotes terms that are $\mathcal{O}(e^{-2\kappa_0 L})$ and higher. A χ^2-minimization fit to the deuteron binding energies in Table VI generates the region in $c_1 - B_d^{(\infty)}$ parameter space shown in Fig. 12, defined by $\chi^2 \to \chi^2_{\rm min} + 1$. The deuteron binding energy found from extrapolating to infinite volume is

$$B_d^{(\infty)} = 14.4^{+(1.6)(2.7)(0.2)(0.2)}_{-(1.8)(1.8)(0.2)(0.2)}\ \text{MeV}. \tag{12}$$

The first uncertainty corresponds to the statistical uncertainty, the second corresponds to the fitting systematic uncertainty, the third is associated with scale setting and the last uncertainty is introduced by the finite-volume extrapolation in Eq. (11), and is estimated by considering the effect of terms scaling as $\sim e^{-2\kappa_0 L}/L$. Combining the errors in Eq. (12) in quadrature leads to $B_d^{(\infty)} = 14.4^{+3.2}_{-2.6}$ MeV.

TABLE VI. The deuteron binding energies extracted from plateaus in the EMPs shown in Fig. 11, along with the infinite-volume extrapolated value. The size of the FV effects is characterized by $e^{-\kappa L}$, shown in the last column. The first uncertainty corresponds to the statistical uncertainty associated with the fit, the second corresponds to the systematic uncertainty associated with the selection of the fitting interval (determined by varying this range). In the case of dimensionful quantities, the third uncertainty is associated with scale setting. For the infinite-volume values of the binding energy, the last uncertainty is introduced by the finite-volume extrapolation in Eq. (11), and is estimated by considering the effect of omitted terms scaling as $e^{-2\kappa_0 L}/L$.

Ensemble	ΔE (l.u.)	B_d (MeV)	$e^{-\kappa L}$
$24^3 \times 64$	−0.01157(73)(96)	19.6(1.2)(1.6)(0.2)	0.111
$32^3 \times 96$	−0.01037(89)(96)	17.5(1.5)(1.6)(0.2)	0.063
$48^3 \times 96$	−0.0078(12)(19)	13.3(2.0)(3.2)(0.2)	0.027
$L = \infty$	$-0.0085^{+(10)(16)(01)}_{-(10)(11)(01)}$	$14.4^{+(1.6)(2.7)(0.2)(0.2)}_{-(1.8)(1.8)(0.2)(0.2)}$	

1. The mixing parameter, ϵ_1

For a deuteron that is moving in the lattice volume, the energy eigenvalues are sensitive to the mixing parameter ϵ_1, as expected from the QCs given in Eq. (9) for the specific boost $\mathbf{d} = (0, 0, 1)$. Explicitly evaluating the $c^{\mathbf{d}}_{lm}$ functions that appear in Eq. (9) for the two irreps containing the deuteron gives the QCs,

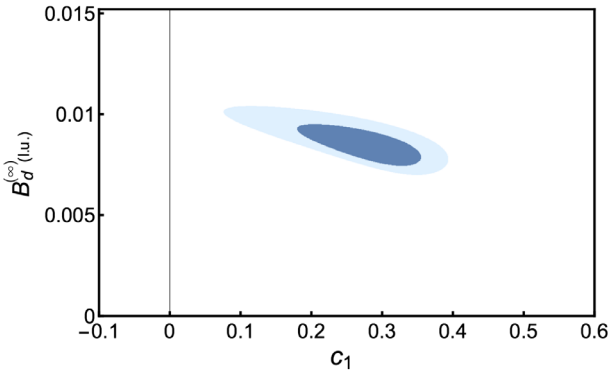

FIG. 12 (color online). The region in $c_1 - B_d^{(\infty)}$ parameter space defined by $\chi^2 \to \chi^2_{\rm min} + 1$. The inner region is defined by the statistical uncertainty, while the outer region is defined by the statistical and systematic uncertainties combined in quadrature.

$$k^*_{\mathbb{A}_2}\cot\delta_{1\alpha}(i\kappa_{\mathbb{A}_2}) + \kappa_{\mathbb{A}_2} = \frac{2e^{-\kappa_{\mathbb{A}_2}L}}{L}\left[1 + 2\left(1 + \frac{3}{\kappa_{\mathbb{A}_2}L} + \frac{3}{(\kappa_{\mathbb{A}_2}L)^2}\right)s_{\epsilon_1}(i\kappa_{\mathbb{A}_2})\right],$$

$$k^*_{\mathbb{E}}\cot\delta_{1\alpha}(i\kappa_{\mathbb{E}}) + \kappa_{\mathbb{E}} = \frac{2e^{-\kappa_{\mathbb{E}}L}}{L}\left[1 - \left(1 + \frac{3}{\kappa_{\mathbb{E}}L} + \frac{3}{(\kappa_{\mathbb{E}}L)^2}\right)s_{\epsilon_1}(i\kappa_{\mathbb{E}})\right], \quad (13)$$

where $s_{\epsilon_1}(k^*)$ is defined in Eq. (10). For both irreps, the functions $k^*\cot\delta$ and s_{ϵ_1} are evaluated at $k^* = i\kappa$. Iteratively solving these QCs in terms of the infinite-volume binding momentum, κ_0 ($\kappa_{\mathbb{A}_2}$, $\kappa_{\mathbb{E}} \to \kappa_0$ in the infinite-volume limit), the spin-averaged binding energy of the $\mathbb{A}_2$ and $\mathbb{E}$ irreps is

$$\bar{B}_d^{(0,0,1)} = B_d^{(\infty)} + \frac{4\kappa_0}{M}\frac{Z_\psi^2}{L}e^{-\kappa_0 L} + \cdots, \quad (14)$$

where the ellipsis denotes terms $\mathcal{O}(e^{-\sqrt{2}\kappa_0 L})$ and higher, which is consistent, at this order, with the binding energy extracted from the $\mathbb{T}_1$ irrep for the deuteron at rest. In the above expression, Z_ψ^2 is the residue of the deuteron pole. The difference in energies is

$$\delta B_d^{(0,0,1)} = -\frac{12\kappa_0}{M}\frac{Z_\psi^2}{L}e^{-\kappa_0 L}\left(1 + \frac{3}{\kappa_0 L} + \frac{3}{(\kappa_0 L)^2}\right)s_{\epsilon_1}(i\kappa_0) + \ldots. \quad (15)$$

Calculating the exponentially small difference between the energies of these two states provides a direct measure of ϵ_1 evaluated at the deuteron pole. In order to extract a meaningful constraint on ϵ_1, the FV corrections must be statistically different from zero, otherwise the coefficient of the leading contribution to the energy difference vanishes.

In the present production, it has been only possible to decompose the $\mathbf{d} = (0,0,1)$ boosted deuteron correlation functions into the $\mathbb{E}$ ($j_z = \pm 1$) and $\mathbb{A}_2$ ($j_z = 0$) irreps in calculations performed with the $L = 32$ ensemble. The EMP associated with the difference in energies between these irreps is shown in Fig. 13, and the energy difference extracted from fitting the plateau region is consistent with zero, $\delta B_d^{(0,0,1)}(L = 32) = -0.4(4.1)(4.6)$ MeV. While this energy difference is bounded in magnitude, the fact that the FV contributions to the deuteron binding energy are consistent with zero in this lattice volume means that no useful bound can be placed upon ϵ_1.

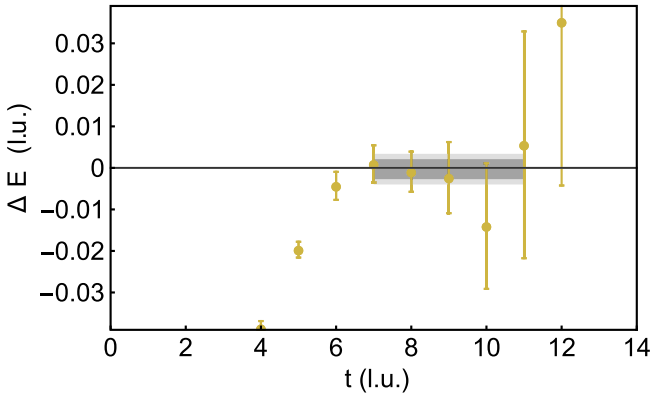

FIG. 13 (color online). EMP associated with the energy difference between the $\mathbb{E}$ ($j_z = \pm 1$) and $\mathbb{A}_2$ ($j_z = 0$) deuteron states with boost vector $\mathbf{d} = (0,0,1)$ in the $L = 32$ ensemble, along with fits to the plateau region. The energy difference depends upon the mixing parameter ϵ_1.

2. A compilation of deuteron binding energies from LQCD

The current calculation of the deuteron binding energy adds to a small number of previous calculations over a range of pion masses above ~300 MeV [11,14,15,21],[3] as shown in Fig. 14.[4] The present result is consistent, within uncertainties, with the results at $m_\pi \sim 300$ MeV and $m_\pi \sim 500$ MeV from Refs. [15,21]. Further LQCD calculations at lighter quark masses are required to quantify the approach to the physical deuteron binding (for related NNEFT work see Ref. [28]).

B. Scattering in the $^3S_1 - {}^3D_1$ coupled channels

To recover the S-matrix in the $^3S_1 - {}^3D_1$ coupled channels, calculations must be performed that isolate the phase shifts and mixing angle, $\delta_{1\alpha}$, ϵ_1 and $\delta_{1\beta}$, defined in Eq. (7), from the FV observables accessible to LQCD calculations. The formalism with which to perform this analysis [51,58–60] is an extension of the seminal work of Lüscher [53,54]. For vanishing total momentum, assuming that the contribution from $\delta_{1\beta}$, D-waves and higher are negligible, the energies of the $\mathbb{T}_1$ irreps are insensitive to ϵ_1, as demonstrated in Eq. (8). Therefore, the shifts in energies of the two nucleon states in the $\mathbb{T}_1$ irrep for various total momentum from the energy of two free nucleons can be used to extract $\delta_{1\alpha}$ below the inelastic threshold.

Figure 15 show the effective-k^{*2} plots (Ek2Ps) associated with the first continuum $\mathbb{T}_1$ states in each ensemble, with momentum near $k^* = 2\pi/L$. These show the values of the interaction momentum k^{*2} extracted from the LQCD correlation functions as a function of Euclidean time. As with the EMPs, plateau behavior indicates the dominance of a single state. Because of the $\mathbb{E}$ irrep of the cubic group

[3]The deuteron and dineutron binding energies at $m_\pi \sim 800$ MeV in the $L = 24$ and $L = 32$ ensembles presented in Ref. [14] have been reproduced in Ref. [22], within uncertainties, on the same gauge ensembles.

[4]The results of quenched calculations, and of calculations that have not been extrapolated to infinite volume [2], have not been shown. The results from Ref. [15,21] were obtained with a power-law extrapolation to infinite volume. This is not the correct form for a loosely bound state, and tends to lead to significantly smaller uncertainties than from extrapolations performed with the known exponential form.

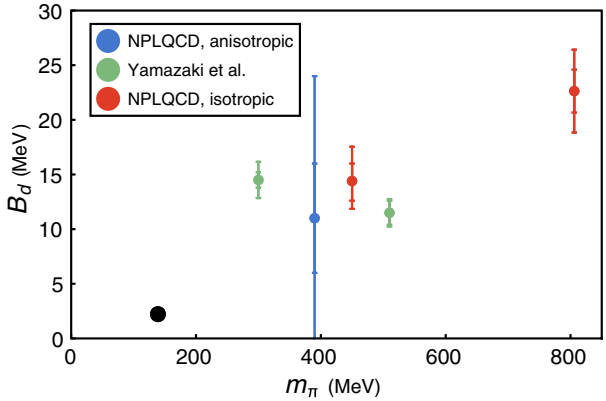

FIG. 14 (color online). The pion-mass dependence of the deuteron binding energy calculated with LQCD. The NPLQCD anisotropic-clover result is from Ref. [11], the Yamazaki *et al.* results are from Refs. [15,21] and the NPLQCD isotropic-clover results are from this work and Ref. [14]. The black disk corresponds to the experimental binding energy.

that is present in the $k^* = 2\pi/L$ shell, the spectrum is expected to have a predominantly D-wave state that is close to [51]. The overlap of our sources and sinks onto this state will be small, dictated by the small mixing between the S-waves and D-waves. Analogous states are also present in higher-k^* shells and in boosted systems. For an arbitrary two-body system, comprised of particles with masses m_1 and m_2, with zero CoM momentum, the interaction momentum k^{*2} is defined through

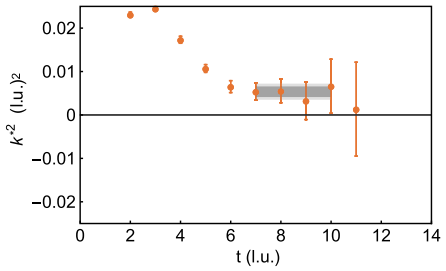

FIG. 17 (color online). Ek2Ps for the spin-averaged continuum ${}^3S_1 - {}^3D_1$ NN states with $\mathbf{d} = (0,0,1)$ near $k^* = 0$ in the $L = 32$ ensemble, along with the fit to the plateau region.

$$\delta E^* = E^* - m_1 - m_2 = \sqrt{k^{*2} + m_1^2} + \sqrt{k^{*2} + m_2^2} - m_1 - m_2, \quad (16)$$

where E^* is the energy in the CoM frame, defined by $E^* = \sqrt{E^2 - |\mathbf{P}_{\rm tot}|^2}$, where E is the total energy, and $\mathbf{P}_{\rm tot}$. is the total momentum, of the system. Figure 16 shows the Ek2Ps for states with momentum near $k^* = 2\sqrt{2}\pi/L$, while Fig. 17 shows the Ek2P for the system with $\mathbf{d} = (0,0,1)$ on the $L = 32$ ensemble. Inserting the values of k^* extracted from the plateau regions of the Ek2Ps in Figs. 15 and 16 into the QC in Eq. (8) gives rise to the values of $k^* \cot\delta_{1\alpha}$ and $\delta_{1\alpha}$ given in Table VII and shown in Fig. 18. Additionally, the result of inserting the value of k^* extracted from the plateau in Fig. 17 into the QC for the $\mathbb{A}_2$ and $\mathbb{E}$ irreps in Eq. (9) is shown in Table VII and Fig. 18. The uncertainties in each of the extractions are relatively large,

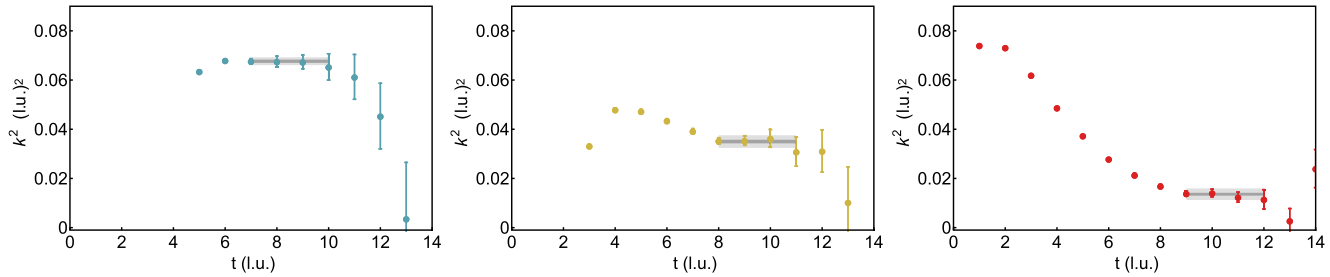

FIG. 15 (color online). Ek2Ps for the lowest-lying continuum ${}^3S_1 - {}^3D_1$ NN states near $k^* = 2\pi/L$ in the $L = 24$ (left panel), $L = 32$ (center panel) and $L = 48$ (right panel) ensembles, along with fits to the plateau regions.

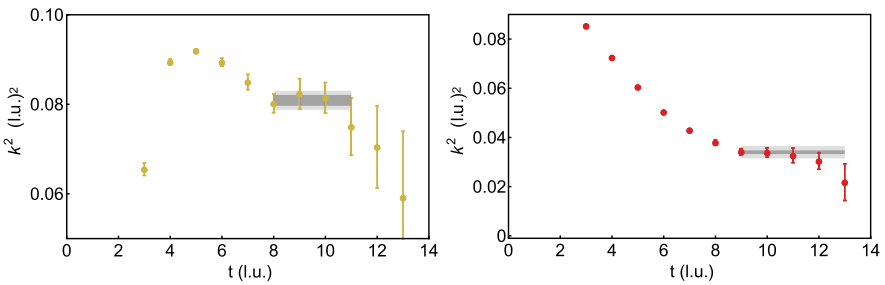

FIG. 16 (color online). Ek2Ps for the continuum ${}^3S_1 - {}^3D_1$ NN states near $k^* = 2\sqrt{2}\pi/L$ in the $L = 32$ (left panel) and $L = 48$ (right panel) ensembles, along with fits to the plateau regions.

TABLE VII. Scattering information in the $^3S_1 - {}^3D_1$ coupled channels. Center dots indicate that the uncertainty extends across a singularity of the Lüscher function, or that it is associated with the bound state. The uncertainties in these quantities are highly correlated, as can be seen from Fig. 18.

Ensemble	$\lvert\mathbf{P}_{\rm tot}\rvert$ (l.u.)	k^*/m_π	$k^*\cot\delta_{1\alpha}/m_\pi$	$\delta_{1\alpha}$ (degrees)
All	0	$i0.294^{+(17)(27)}_{-(18)(24)}$	$-0.294^{+(17)(27)}_{-(18)(24)}$	…
$24^3\times64$	0	$0.9754^{+(44)(98)}_{-(45)(99)}$	…	3.1(1.7)(3.7)
$32^3\times96$	0	$0.702^{+(10)(23)}_{-(10)(24)}$	$2.3^{+(1.0)(5.7)}_{-(0.55)(0.89)}$	17(5)(11)
$32^3\times96$	0	$1.065^{+(07)(16)}_{-(08)(17)}$	$-5.4^{+(1.4)(2.1)}_{-(2.9)(29.5)}$	−11.1(3.8)(8.5)
$32^3\times96$	1	$0.270^{+(26)(29)}_{-(40)(51)}$	$+0.35^{+(24)(15)}_{-(59)(20)}$	$+38^{+(13)(23)}_{-(11)(16)}$
$48^3\times96$	0	0.426(03)(12)	$0.45^{+(67)(34)}_{-(26)(08)}$	$44^{+(21)(07)}_{-(21)(08)}$
$48^3\times96$	0	0.662(08)(29)	$0.35^{+(0.14)(3.0)}_{-(0.09)(0.21)}$	$26^{+(07)(25)}_{-(07)(22)}$

magnified by their close proximity to a singularity in the kinematic functions $c_{00}^{\mathbf{d}}$. Even subject to these issues, a zero in the phase shift is visible near $k^* \sim m_\pi \sim 450$ MeV, indicative of an attractive interaction with a repulsive core. It is interesting to compare this phase shift, at a pion mass of $m_\pi \sim 450$ MeV, with that of nature, illustrated by the dashed curve in Fig. 18. The phase shift resulting from a partial-wave analysis of experimental data is consistent, within uncertainties, with the phase shift calculated at $m_\pi \sim 450$ MeV over a large range of momenta. The zeros of the phase shift occur at different momenta, but they are nearby. Without results at smaller k^*, a precise extraction of the scattering parameters, such as the scattering length and effective range, is not feasible, and additional calculations are required in order to accomplish this. However, the determination of the binding energy and the two continuum states that lie below the threshold of the t-channel cut (set by the pion mass, $k^* = m_\pi/2$) can be used to perform an approximate determination of the inverse scattering length and effective range. A linear fit was performed, $k^*\cot\delta = -1/a + \frac{1}{2}rk^{*2}$, as shown in Fig. 19. The range of linear fits straddle $k^*\cot\delta = 0$ at $k^* = 0$, and as such allows both $a^{(^3S_1)} = \pm\infty$, and it is useful to consider the constraints on $1/a^{(^3S_1)}$ rather than $a^{(^3S_1)}$. The correlated constraints on $1/a^{(^3S_1)}$ and $r^{(^3S_1)}$ are shown in Fig. 19. The inverse scattering length and effective range determined from the fit region in Fig. 19 are

$$\begin{aligned}(m_\pi a^{(^3S_1)})^{-1} &= -0.04^{+(0.07)(0.08)}_{-(0.10)(0.17)},\\ m_\pi r^{(^3S_1)} &= 7.8^{+(2.2)(3.5)}_{-(1.5)(1.7)}\\ (a^{(^3S_1)})^{-1} &= -0.09^{+(0.15)(0.19)}_{-(0.23)(0.39)}\ \text{fm}^{-1},\\ r^{(^3S_1)} &= 3.4^{+(1.0)(1.5)}_{-(0.7)(0.8)}\ \text{fm}.\end{aligned} \tag{17}$$

Further calculations in larger volumes (and hence at smaller k^{*2}) will be required to refine these extractions. There is a potential self-consistency issue raised by the size of the effective range that is within the uncertainties that are reported. Lüscher's method is valid only for the interaction ranges $R \ll L/2$, otherwise the exponentially small corrections due to deformation of the interhadron forces become large. Assuming the range of the interaction is of similar size to the effective range (as expected for "natural" interactions), this requirement is not met and deviations from the assumed linear fitting function should be entertained. Higher precision analyses will be required to investigate this further.

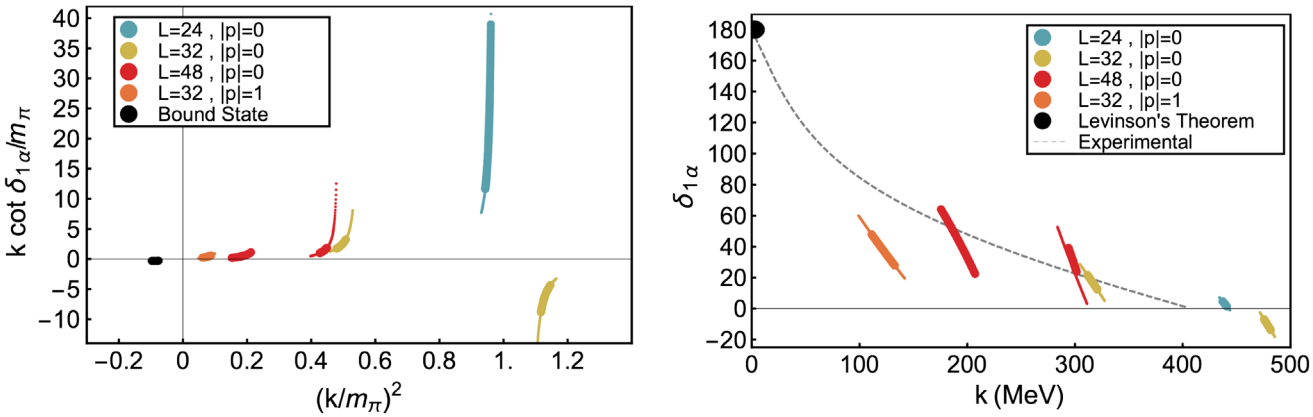

FIG. 18 (color online). Scattering in the $^3S_1 - {}^3D_1$ coupled channels. The left panel shows $k^*\cot\delta_{1\alpha}/m_\pi$ as a function of k^{*2}/m_π^2, while the right panel shows the phase shift as a function of momentum in MeV, assuming that $\delta_{1\beta}$ and the D-wave and higher partial-wave phase shifts vanish. The thick (thin) region of each result corresponds to the statistical uncertainty (statistical and systematic uncertainties combined in quadrature). The black circle in the right panel corresponds to the known result from Levinson's theorem, while the dashed-gray curve corresponds to the phase shift extracted from the Nijmegen partial-wave analysis of experimental data [61].

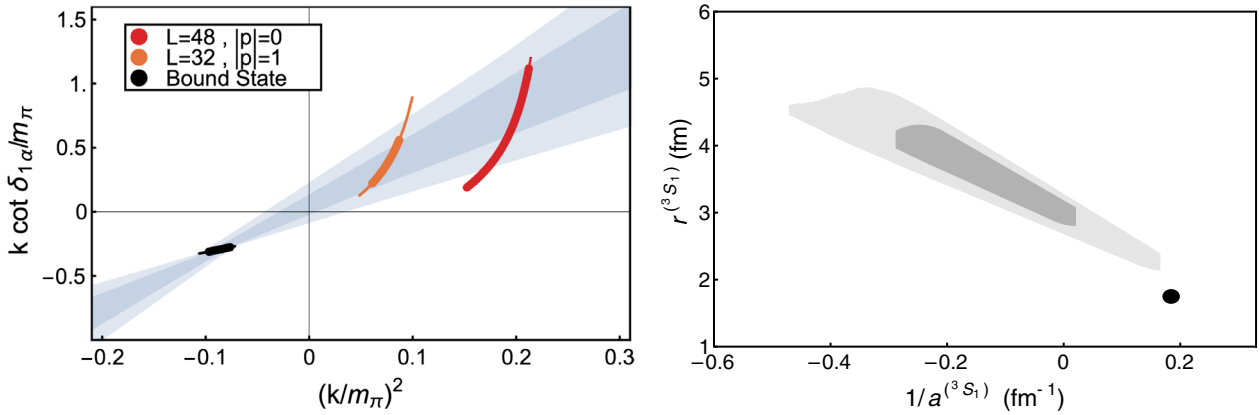

FIG. 19 (color online). Scattering in the ${}^3S_1 - {}^3D_1$ coupled channels below the start of the t-channel cut, $k^{*2} < m_\pi^2/4$, assuming that $\delta_{1\beta}$ and the D-wave and higher partial-wave phase shifts vanish. The left panel shows a solid region corresponding to linear fits associated with the statistical uncertainty and the statistical and systematic uncertainties combined in quadrature. The right panel shows the scattering parameters, $1/a^{(^3S_1)}$ and $r^{(^3S_1)}$ determined from fits to scattering results below the t-channel cut. The solid circle corresponds to the experimental values.

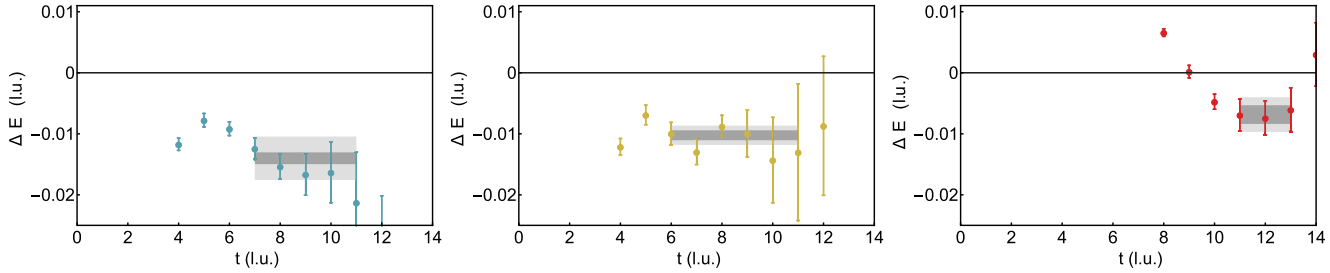

FIG. 20 (color online). EMPs for the dineutron in the $L = 24$ (left panel), $L = 32$ (center panel) and $L = 48$ (right panel) ensembles, along with fits to the plateau regions. The extracted binding energies are given in Table VIII.

V. THE ${}^1S_0$ CHANNEL AND THE DINEUTRON

The analysis of LQCD calculations in the ${}^1S_0$ channel are somewhat simpler than in the ${}^3S_1 - {}^3D_1$ coupled channels, as scattering below the inelastic threshold is described by a single phase shift, $\delta^{({}^1S_0)}$. In FV, the relation between energy eigenvalues of the system at rest in the $\mathbb{A}_1$ cubic irrep and $\delta^{({}^1S_0)}$ are given by Eq. (8) with $\delta_{1\alpha} \to \delta^{({}^1S_0)}$ and $k^*_{\mathbb{T}_1} \to k^*_{\mathbb{A}_1}$. Unfortunately, the correlation functions in this channel have larger fluctuations and excited state contamination than those in the ${}^3S_1 - {}^3D_1$ coupled-channel system. Consequently, the uncertainties associated with each energy level are larger.

A. The dineutron

Unlike in nature, the dineutron is found to be bound at heavier quark masses [14,15,17,19,21] by direct calculations of the ground-state energies of two nucleons in finite lattice volumes.[5] Plateaus identified with a negatively shifted dineutron were found in all three ensembles, with the associated EMPs shown in Fig. 20 and the extracted energy shifts shown in Table VIII. Performing a volume extrapolation using the form given in Eq. (11) leads to a binding energy of[6]

$$B_{nn}^{(\infty)} = 12.5^{+(1.7)(2.5)(0.2)(0.2)}_{-(1.9)(4.5)(0.2)(0.2)}\ \text{MeV}. \tag{18}$$

Combining the errors in Eq. (18) in quadrature leads to $B_{nn}^{(\infty)} = 12.5^{+3.0}_{-5.0}$ MeV. The $c_1 - B_{nn}^{(\infty)}$ parameter space defined by $\chi^2 \to \chi^2_{\text{min}} + 1$ determined from an uncorrelated fit to the dineutron binding energies in the three volumes is shown in Fig. 21. This dineutron binding energy is consistent with the binding energy of the deuteron within uncertainties. The EMPs associated with the difference between the deuteron and dineutron energies in each ensemble are shown in Fig. 22, resulting in the energy

[5]The HAL QCD method appears not to give rise to a bound deuteron or dineutron at these heavier pion masses, e.g. Ref. [16].

[6]Extrapolating with a form consistent with a scattering state, which would display a volume dependence of $\Delta E \sim 1/L^3$, results in a poor goodness of fit.

TABLE VIII. The dineutron binding energies from fitting to the EMPs shown in Fig. 20.

Ensemble	ΔE (l.u.)	B_{nn} (MeV)	$e^{-\kappa L}$
$24^3 \times 64$	$-0.0142(09)(27)$	$24.1(1.5)(4.5)$	0.088
$32^3 \times 96$	$-0.0109(09)(20)$	$18.4(1.5)(3.3)$	0.058
$48^3 \times 96$	$-0.0070(11)(18)$	$11.8(1.9)(3.1)$	0.033
$L = \infty$	$-0.0074^{+(10)(15)(01)}_{-(11)(27)(01)}$	$12.5^{+(1.7)(2.5)(0.2)(0.2)}_{-(1.9)(4.5)(0.2)(0.2)}$	

differences given in Table IX. No significant difference has been extracted.

1. A compilation of dineutron binding energies from LQCD

The current calculation of the dineutron binding energy adds to a small number of previous calculations, a compilation of which is shown in Fig. 23. There does not appear to be a clear pattern emerging as to how the dineutron will unbind as the pion mass is reduced. The results that have been obtained in Refs. [15,21] have consistently smaller uncertainties than those found in Ref. [11,14] and in the present work. However, the results are consistent within the uncertainties.

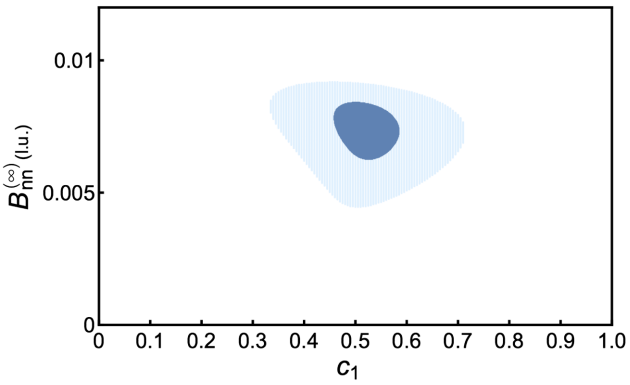

FIG. 21 (color online). The region in $c_1 - B_{nn}^{(\infty)}$ parameter space defined by $\chi^2 \to \chi^2_{\rm min} + 1$. The inner region is defined by the statistical uncertainty, while the outer is defined by the statistical and systematic uncertainties combined in quadrature.

TABLE IX. Energy differences between the dineutron and the deuteron from fitting to the EMPs shown in Fig. 22. All differences are consistent with zero, as is their infinite-volume extrapolation.

Ensemble	$E_{\rm nn} - E_{\rm deut}$ (l.u.)	$E_{\rm nn} - E_{\rm deut}$ (MeV)
$24^3 \times 64$	$+0.0022(16)(28)$	$+3.7(2.8)(4.7)(0.0)$
$32^3 \times 96$	$-0.0014(09)(15)$	$-2.4(1.6)(2.5)$
$48^3 \times 96$	$+0.0027(04)(31)$	$+4.6(0.7)(5.3)$

B. Scattering in the $^1S_0$ channel

Correlation functions for two nucleons in the $^1S_0$ state were constructed in the $\mathbb{A}_1$ irrep of the cubic group. The Ek2Ps associated with the states near the $k^* = 2\pi/L$ and $k^* = 2\sqrt{2}\pi/L$ noninteracting levels are shown in Figs. 24 and 25, respectively. For the lowest-lying "continuum" state, plateaus were found in all three ensembles, however, only the $L = 32$ ensemble has correlation functions that were sufficiently clean to extract the next higher level. A plateau was also identified in the system with one unit of total momentum, as shown in Fig. 26. The values of $k\cot\delta^{(^1S_0)}$ and the phase shift are given in Table X and shown in Fig. 27. Many of the qualitative features of the results for the scattering amplitude in this channel are similar to those in the $^3S_1 - {}^3D_1$ coupled channels. A zero of the phase shift near $k \sim m_\pi \sim 450$ MeV is evident and occurs quite close to the zero of the phase shift in nature. However for $k < 100$ MeV, the $^1S_0$ phase shift at $m_\pi \sim 450$ MeV and in nature become significantly different. In Fig. 28, a linear fit is shown to the three results below the start of the t-channel cut, with the extracted correlated constraints on the scattering parameters also shown. The inverse scattering length and the effective range determined from the fit region in Fig. 28 are

$$(m_\pi a^{(^1S_0)})^{-1} = 0.021^{+(28)(32)}_{-(36)(63)}, \quad m_\pi r^{(^1S_0)} = 6.7^{+(1.0)(2.0)}_{-(0.8)(1.3)}$$
$$(a^{(^1S_0)})^{-1} = 0.05^{+(06)(08)}_{-(08)(14)}\ \text{fm}^{-1}, \quad r^{(^1S_0)} = 2.96^{+(43)(87)}_{-(34)(55)}\ \text{fm}. \tag{19}$$

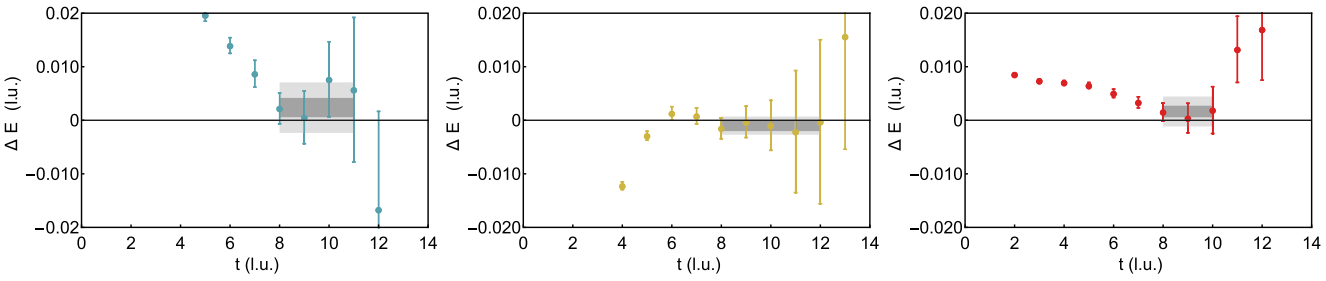

FIG. 22 (color online). EMPs for the energy difference between the dineutron and the deuteron in the $L = 24$ (left panel), $L = 32$ (center panel) and $L = 48$ (right panel) ensembles, along with fits to the plateau regions.

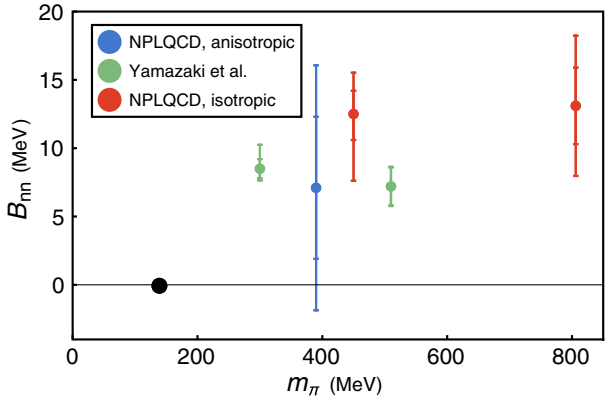

FIG. 23 (color online). The pion-mass dependence of the dineutron binding energy calculated with LQCD. The NPLQCD anisotropic-clover result is from Ref. [11], the Yamazaki *et al.* results are from Refs. [15,21] and the NPLQCD isotropic-clover results are from this work and Ref. [14]. The black disk corresponds to the location of the near-bound state at the physical quark masses.

The allowed region of scattering parameters is shown in Fig. 28 and is close to containing the experimentally determined scattering length and effective range. Since the quark masses are unphysical, the physical values need not be contained in this region and it is interesting how close the current results are to those in nature. As in the ${}^3S_1 - {}^3D_1$ coupled-channel system analyzed in the previous section, there is a potential self-consistency issue raised by the region of the extracted effective range.

VI. OBSERVATIONS ABOUT NUCLEON-NUCLEON EFFECTIVE FIELD THEORY ANALYSES

A modern approach to low-energy nuclear physics rests upon the chiral nuclear forces arising from a nontrivial extension of χPT into the multinucleon sector (see, for instance, Refs. [62–64]). Because of the small scales in the two nucleon systems ($\gamma_d \sim 45$ MeV and $|\gamma_{nn}| \sim 8$ MeV), the NNEFTs are more complicated than a simple expansion in quark masses and momenta that defines χPT, and there are additional dynamics that must be considered. Following

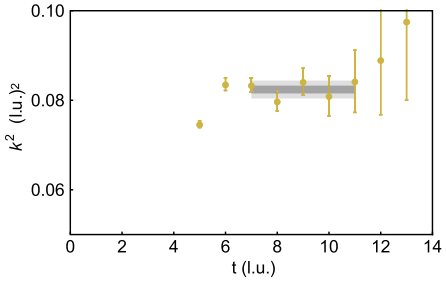

FIG. 25 (color online). Ek2P for the lowest-lying continuum ${}^1S_0$ NN state near $k^* = 2\sqrt{2}\pi/L$ in the $L = 32$ ensemble, along with the fit to the plateau region.

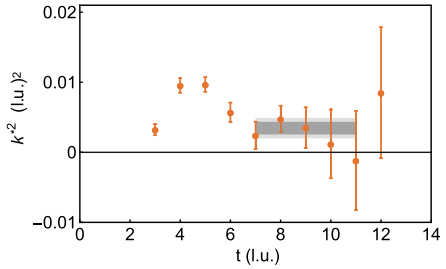

FIG. 26 (color online). Ek2P for the continuum ${}^1S_0$ NN states with $\mathbf{d} = (0, 0, 1)$ near $k^* = 0$ in the $L = 32$ ensemble, along with the fit to the plateau region.

the initial developments by Weinberg [65–67], much effort has gone into understanding the construction and behavior of these theories.

NNEFTs provide a powerful means with which to analyze the momentum and quark-mass dependences of the phase shifts and it is illuminating to consider the LQCD results presented in this work in their context. As is appropriate, we use Kaplan-Savage-Wise (KSW) power counting [68–70] in the ${}^1S_0$ channel and Beane-Bedaque-Savage–van Kolck (BBSvK) power counting [71], a variant of Weinberg's power counting [65,66], in the ${}^3S_1 - {}^3D_1$ coupled channels. There are a number of reasons to undertake this investigation. The chiral decomposition of nuclear forces automatically requires the introduction of terms that are only distinguishable through variation of the

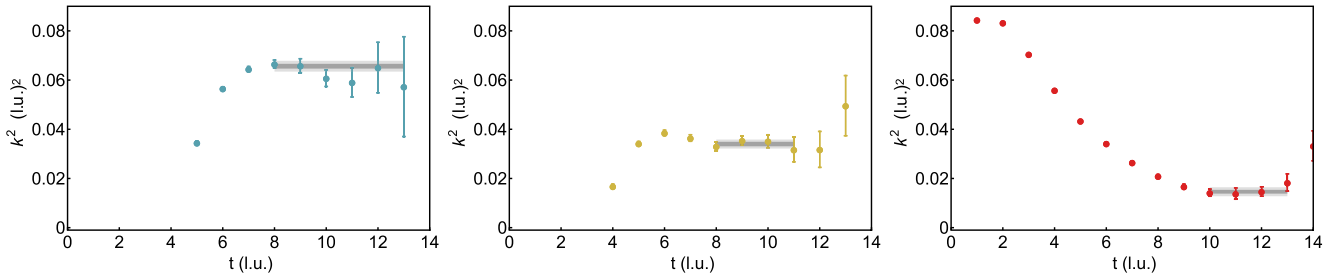

FIG. 24 (color online). Ek2Ps for the lowest-lying continuum ${}^1S_0$ NN state near $k^* = 2\pi/L$ in the $L = 24$ (left panel), $L = 32$ (center panel) and $L = 48$ (right panel) ensembles, along with fits to the plateau regions.

TABLE X. Scattering information in the $^1S_0$ channel. The uncertainties are highly correlated, as can be seen from Fig. 27.

Ensemble	$\lvert\mathbf{P}_{\rm tot}\rvert$ (l.u.)	k^*/m_π	$k^*\cot\delta^{(^1S_0)}/m_\pi$	$\delta^{(^1S_0)}$ (degrees)
All	0	$i0.274^{+(19)(26)}_{-(20)(44)}$	$-0.274^{+(19)(26)}_{-(20)(44)}$	⋯
$24^3 \times 64$	0	$0.954^{+(08)(18)}_{-(08)(19)}$	$5.0^{+(2.0)(10.0)}_{-(1.1)(1.8)}$	$10.8^{+(3.0)(6.5)}_{-(3.0)(6.7)}$
$32^3 \times 96$	0	$0.691^{+(09)(16)}_{-(09)(16)}$	$1.7^{+(0.5)(1.1)}_{-(0.3)(0.5)}$	$22.0^{+(4.2)(7.0)}_{-(4.2)(7.2)}$
$32^3 \times 96$	0	$1.079^{+(05)(10)}_{-(05)(10)}$	$-3.3^{+(0.4)(0.7)}_{-(0.6)(1.5)}$	$-18.3(2.6)(5.2)$
$32^3 \times 96$	1	$0.220^{+(28)(32)}_{-(32)(42)}$	$0.13^{+(10)(14)}_{-(08)(08)}$	$60^{+(14)(20)}_{-(12)(14)}$
$48^3 \times 96$	0	0.453(11)(29)	$0.89^{+(39)(3.7)}_{-(23)(44)}$	$27^{+(07)(18)}_{-(07)(20)}$

quark masses. Comparison of LQCD calculations at unphysical masses allows this previously unavailable "dial" to be turned in the dual expansion that defines chiral NNEFTs. Second, the full decomposition of the chiral NN forces, and thereby precise predictions for nuclear observables, requires knowledge of the mass dependence discussed above and it is essential that such calculations be performed to maximize the predictive power of NNEFTs. Third, the current calculations enable an exploration of the convergence of NNEFTs with pions included as explicit degrees of freedom at relatively large pion masses.

The quality and kinematic coverage of scattering results that have been presented is not yet sufficient to perform a comprehensive analysis of NNEFT matching to LQCD. Instead, we present a simplified discussion of the two channels to highlight some of the important features and questions that will need to be addressed in order to accomplish a reliable determination of the chiral nuclear forces from LQCD. Related discussions in the context of pionless EFTs for multinucleon systems can be found in Refs. [72,73] and implicitly in the presentation of the effective range expansion above.

A. KSW analysis of the $^1S_0$ channel

The KSW power counting [68–70] provides a rigorous framework with which to perturbatively expand the two nucleon scattering amplitude in the $^1S_0$ channel in the two small-expansion parameters, nominally p/Λ_{NN} and m_π/Λ_{NN}. Here $\Lambda_{NN} = 8\pi f_\pi^2/g_A^2 M_N$ is the natural scale of validity of the NNEFT. At the physical point $\Lambda_{NN} \sim 289$ MeV, while at a pion mass of 450 MeV it is $\Lambda_{NN} \sim 350$ MeV. These scales should be compared with the start of the t-channel cut from the next lightest meson, $m_\rho/2 \sim 385$ MeV at the physical point, and $m_\rho/2 \sim 443$ MeV at a pion mass of 450 MeV. This power counting treats the zero-derivative two nucleon operator nonperturbatively, and was developed in order to correctly define a theory that is finite and renormalization group invariant at each order in the expansion. An analysis of nucleon-nucleon (NN) interactions at the physical point has been carried out to next-to-next-to-leading order (NNLO) in the KSW expansion [68,69,74–76], and we have performed the analogous analysis of the present LQCD results. The leading order (LO), next-to-leading order (NLO) and NNLO amplitudes in the $^1S_0$ channel can be found in Refs. [68,69,74,75], along with the relevant expansion of the phase shift. At LO, there is only one fit parameter, constrained by the location of the dineutron pole. At NLO, there are nominally two additional fit parameters, but requiring that the dineutron pole remains unchanged reduces the number to one, ξ_1, while the other, ξ_2, can be directly related to ξ_1. Finally, at NNLO there are three more parameters, but only one parameter, ξ_4, is independent for similar reasons as at NLO. Therefore, there are only three fit parameters for a complete analysis at NNLO.

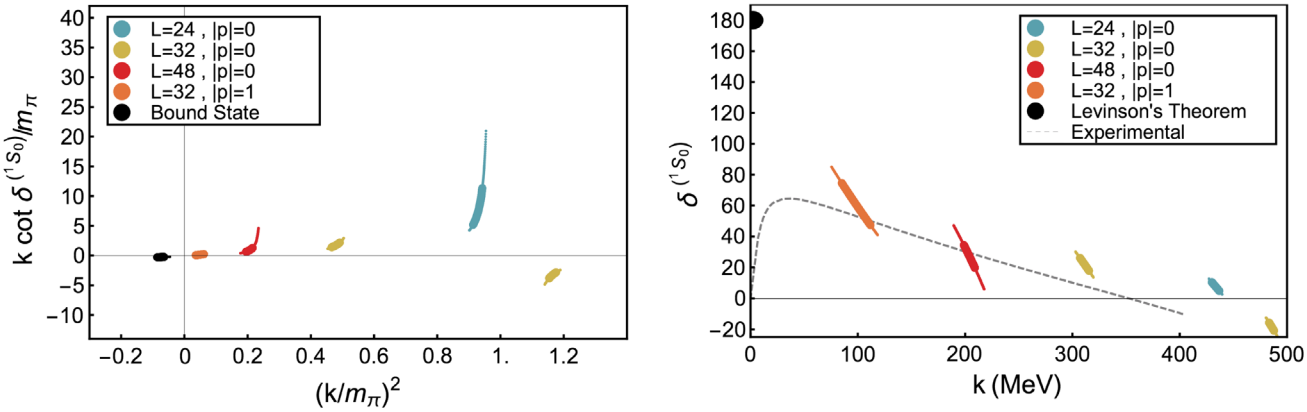

FIG. 27 (color online). Scattering in the $^1S_0$ channel. The left panel shows $k^*\cot\delta^{(^1S_0)}/m_\pi$ as a function of k^{*2}/m_π^2, while the right panel shows the phase shift as a function of momentum in MeV. The thick (thin) region of each result corresponds to the statistical uncertainty (statistical and systematic uncertainties combined in quadrature). The black circle in the right panel corresponds to the known bound-state result from Levinson's theorem, while the dashed-gray curve corresponds to the phase shift extracted from the Nijmegen partial-wave analysis of experimental data [61].

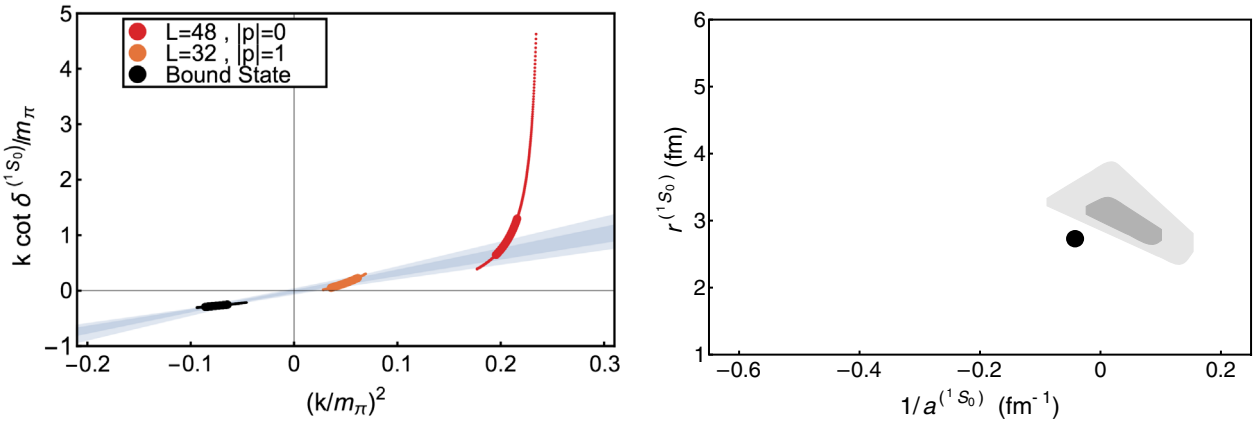

FIG. 28 (color online). Scattering in the $^1S_0$ channel below the start of the t-channel cut, $k^{*2} < m_\pi^2/4$. The left panel shows the linear fit with the darker and lighter shaded regions associated with the statistical uncertainty and the statistical and systematic uncertainties combined in quadrature. The right panel shows the scattering parameters, $1/a^{(^1S_0)}$ and $r^{(^1S_0)}$, determined from fits to scattering results below the t-channel cut. The solid circle corresponds to the experimental values.

Results of fitting the LO, NLO and NNLO phase shifts are shown in Fig. 29. The phase shifts at all momenta are utilized in the fits (a more complete analysis would consider the effects of truncations).

Fitting the location of the dineutron bound state, the LO fit is clearly inconsistent with the phase shifts at higher energies, as is also seen in fits at the physical point. At NLO the fit is quite reasonable at the energies near the zero of the phase shift, but becomes somewhat deficient at lower energies. The NNLO fit is found to move closer to the LQCD results. It appears that the KSW expansion is converging to the LQCD results, but fits beyond NNLO are required to reproduce the LQCD results with an acceptable goodness of fit. The values of $\xi_{1,4}$ are both of natural size, as can be seen in Fig. 29.

The resulting scattering parameters at NLO and NNLO are

$$a_{\rm NLO}^{(^1S_0)} = 2.62(07)(16)\ \text{fm} \quad r_{\rm NLO}^{(^1S_0)} = 1.320(18)(38))\ \text{fm}$$
$$a_{\rm NNLO}^{(^1S_0)} = 2.99(07)(15)\ \text{fm} \quad r_{\rm NNLO}^{(^1S_0)} = 1.611(42)(83))\ \text{fm}, \tag{20}$$

From the differences between orders, it is clear that the systematic uncertainty introduced by the KSW expansion exceeds the uncertainties of the LQCD calculations, and orders beyond NNLO are required to render the "theory error" (from truncating the KSW expansion) small compared with the uncertainties of the calculation. As the KSW expansion is a double expansion in both momentum and the

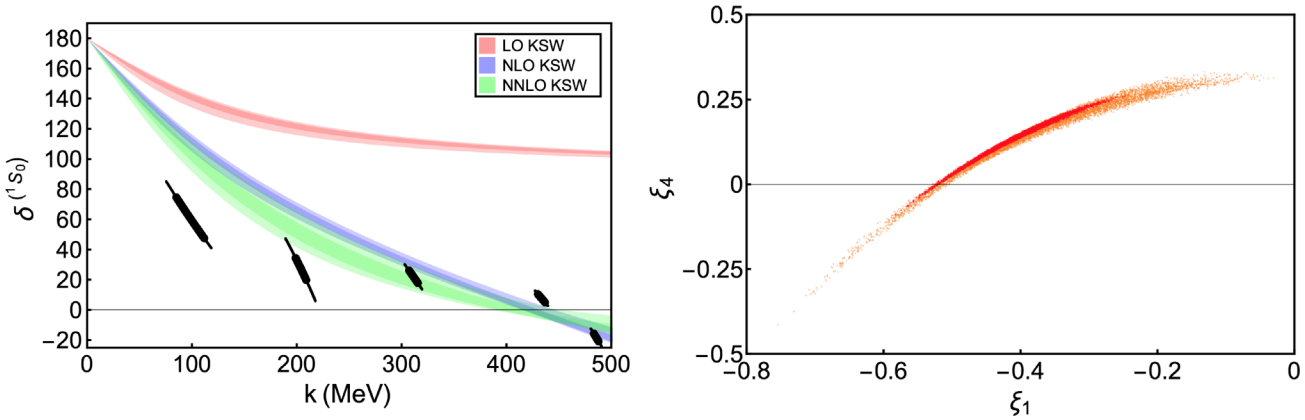

FIG. 29 (color online). The left panel shows the LQCD $^1S_0$ scattering phase shift along with the KSW NNEFT fits at LO, NLO and NNLO. At LO there is one parameter that is fit to recover the dineutron pole, giving the red-shaded region, at NLO there is one additional fit parameter, giving the blue-shaded region, and at NNLO there is a further fit parameter, giving the green-shaded region. The darker (lighter) shaded regions correspond to the statistical (statistical and systematic uncertainties combined in quadrature). The right panel is a scatter plot of the central values of the extracted NNLO fit parameters, $\xi_{1,4}$ over the 1σ range of the dineutron pole. The red- (orange-) shaded region corresponds to the statistical (statistical and systematic uncertainties combined in quadrature).

pion mass, the threshold scattering parameters have chiral expansions order by order in the expansion. The values of the scattering parameters extracted from fitting the KSW expressions differ from those obtained by fitting a truncated effective range expansion to the phase shifts at the lowest two momenta and the dineutron pole, i.e. they do not lie in the region presented in Fig. 28. This may indicate that the KSW expansion should not be applied to the phase shifts over the full range of momenta; indeed the largest two momenta have $k \gtrsim \Lambda_{NN}$. However, removing these points does not change the fit qualitatively due to the relative size of the uncertainties. These results could also indicate that the pion mass is simply too large, as it exceeds Λ_{NN}. However, it does appear that the expansion is converging, albeit slowly, to the calculated phase shifts.

As the calculations have been performed at only one pion mass (previous phase shift calculations at $m_\pi = 806$ MeV [14,17] are expected to be beyond the range of applicability of the NNEFT), it is not possible to isolate the explicit short-distance pion-mass dependence in $\xi_{1,4}$, which both receive contributions from pion-mass independent and pion-mass dependent terms. Hence, a chiral extrapolation to the physical point is not feasible from this work alone. Calculations that are currently under way will provide results at a lower pion mass, from which predictions at the physical point will become possible.

B. BBSvK Analysis of the $^3S_1 - {}^3D_1$ Coupled Channel

BBSvK power counting [71] is similar to Weinberg's power counting [65,66], and is an appropriate scheme to use in the case of the $^3S_1 - {}^3D_1$ coupled channels. A NN interaction (two-particle irreducible) is derived using the familiar rules of χPT and, due to the infrared behavior of the two nucleon system, is iterated to all orders with the Schrödinger equation to generate the bound-state pole(s) and scattering amplitude(s). See Ref. [77] for a review.

At LO in Weinberg's power counting, the NN interactions are determined by momentum-independent and quark-mass-independent two nucleon contact interactions and by one-pion exchange (OPE). However, the short-distance nature of the tensor force, resulting from OPE, generates renormalization-scale dependence in the D-waves that requires the presence of a counterterm at LO, and BBSvK is the simplest power counting to remedy this situation. At NLO in the counting, there are contributions from pion-loop diagrams, from momentum-dependent two nucleon contact interactions, and from insertions of the light-quark mass matrix into momentum-independent two nucleon contact interactions. With the parameters in the meson sector, e.g. g_A, f_π, fixed to the results of other LQCD calculations at similar quark masses, there is one free parameter at LO in BBSvK counting—the coefficient of the momentum-independent two nucleon contact interaction. This is common to both the S-waves and the D-waves.

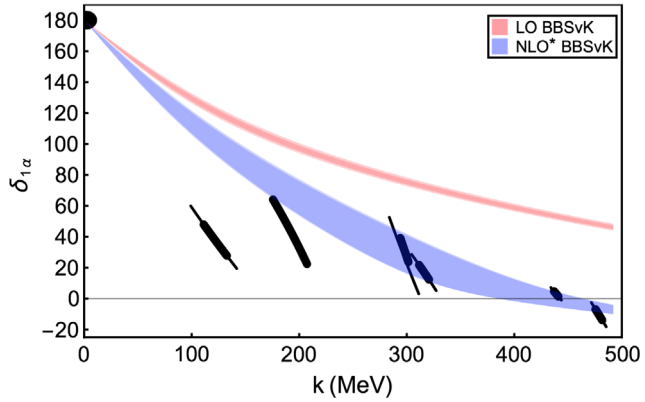

FIG. 30 (color online). The $^3S_1 - {}^3D_1$ coupled-channel scattering phase shift, $\delta_{1\alpha}$, along with BBSvK fits at LO and NLO*. At LO there is one parameter that is fit to recover the deuteron pole, giving the red-shaded region, while at NLO* there is one additional fit parameter, giving the blue-shaded region. The darker (lighter) shaded regions correspond to the statistical (statistical and systematic uncertainties combined in quadrature).

At NLO, the expansion becomes more complicated with different interactions in the S-waves and D-waves. Without being able to separately resolve the $\delta_{1\alpha}$ and $\delta_{1\beta}$ phase shifts, only the common terms can be determined. To this end, we have defined NLO* to be LO with the inclusion of the leading momentum-dependent two nucleon contact interaction that is also common to both the S-waves and the D-waves, but omitting other NLO contributions. NLO* introduces a single additional parameter beyond LO.

The results of fitting the LO and NLO* parameters to the results of our LQCD calculations are shown in Fig. 30.[7] The LO fit to the deuteron binding energy leads to phase shifts that significantly overestimate the LQCD results (this is also seen in analyses at the physical point). However, by including the contact-p^2 interaction, relatively good agreement is found in the NLO* fit to all the LQCD phase-shift extractions, with the exception of the lowest energy point (which we attribute to a downward statistical fluctuation whose significance is likely to be reduced at higher orders in the expansion).

The values of the scattering parameters resulting from the fits are

$$\begin{aligned} a_{\rm LO}^{(^3S_1)} &= 1.94(09)(17)\ \text{fm} \quad r_{\rm LO}^{(^3S_1)} = 0.674(17)(29))\ \text{fm} \\ a_{\rm NLO^*}^{(^3S_1)} &= 2.72(22)(27)\ \text{fm} \quad r_{\rm NLO^*}^{(^3S_1)} = 1.43(12)(13))\ \text{fm}, \end{aligned} \tag{21}$$

[7] A square well with a radius of $R = 0.30$ fm has been used to regulate the interaction at short distances. Previous work [71] shows that the observables have corrections that depend only on positive powers of R (after refitting coefficients), as expected from a Wilsonian renormalization group analysis in the limit $R \to 0$.

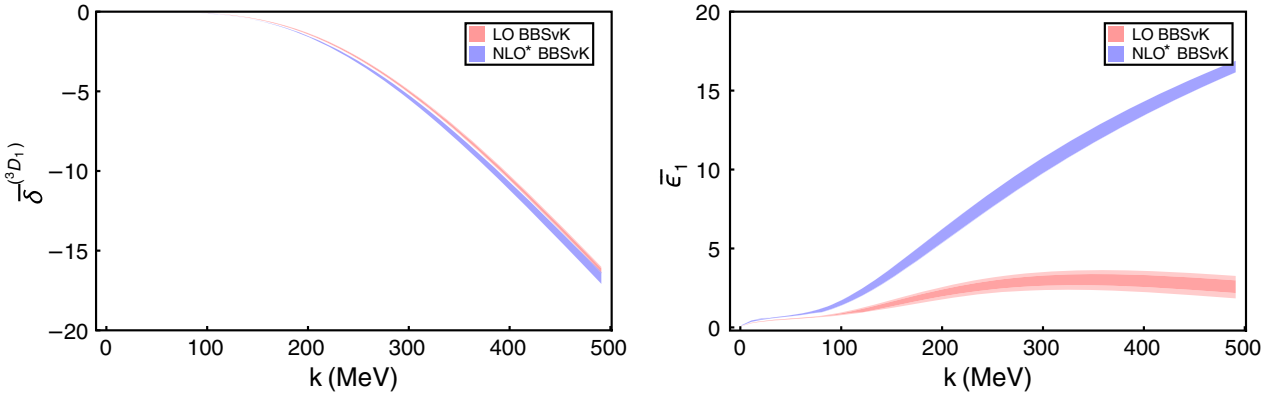

FIG. 31 (color online). The left panel shows the $^3D_1$ scattering phase shift, $\bar{\delta}^{(^3D_1)}$, in the Stapp parametrization [78] along with BBSvK fits at LO and NLO*, while the right panel shows the mixing parameter, $\bar{\epsilon}_1$. The darker (lighter) shaded regions correspond to the statistical (statistical and systematic uncertainties combined in quadrature).

which are consistent, within uncertainties, with those obtained in the $^1S_0$ channel with KSW counting. It is interesting to note that the ratio of scattering length to effective range is $a/r \sim 2$, as was found to be the case at the SU(3) symmetric point [14,17].

A feature of BBSvK counting is that predictions can be made for the mixing parameter, ϵ_1 and $\delta_{1\beta}$, or $\bar{\epsilon}_1$ and $\bar{\delta}^{(^3D_1)}$ in the more familiar Stapp [78] parametrization of the S-matrix. These are shown in Fig. 31, and it is important to keep in mind that the coefficients determined from the deuteron pole and S-wave phase shift contribute to both of these quantities. While the D-wave phase shift is only slightly modified by the NLO* interaction, $\bar{\epsilon}_1$ is changed dramatically. In this initial investigation, the range of the square well interaction has not been varied and estimates of contributions from higher orders have not been included. It is clear that the theory error due to truncation of the BBSvK expansion is large for $\bar{\epsilon}_1$, but not for the D-wave phase shift. In fact, this expansion of $\bar{\epsilon}_1$ is found to be less convergent at this pion mass than at the physical point [71].

VII. CONCLUSIONS

Recovering the experimentally known properties of the two nucleon systems, such as the deuteron bound state, the dineutron virtual-bound state and scattering observables, from QCD represents a major challenge for lattice QCD calculations. Once verified by comparison to known experimental extractions, LQCD calculations hold the promise of refining our knowledge of these systems beyond what is possible experimentally, particularly in the neutron-neutron system and more exotic processes involving hyperons. LQCD calculations have steadily developed in recent years and in the near future calculations of multinucleon systems with physical quark masses will be available [79]. Eventually these calculations will also include the effects of isospin breaking and QED. In this work, we report the results of calculations of nucleon-nucleon interactions in the $^3S_1 - {}^3D_1$ coupled channels and the $^1S_0$ channel at a pion mass of $m_\pi \sim 450$ MeV in three lattice volumes and at a single lattice spacing. The lattice-spacing artifacts are estimated to be small, entering at $\mathcal{O}(\Lambda_{\rm QCD}^2 b^2)$, and are expected to modify the binding energies and phase shifts by amounts that are small compared with the quoted statistical and systematic uncertainties. Both the deuteron and the dineutron are found to be bound at this pion mass, consistent with expectations based upon previous calculations. The phase shifts in both channels are determined at a few discrete momenta and, in both channels, a zero in the phase shift is found to occur near the momentum at which a zero is observed in nature. Calculations of increased precision and kinematic coverage will further our understanding of the two nucleon systems at this set of quark masses. Further calculations at other quark masses will enable direct comparison with experimental extractions and will elucidate important features of the chiral nuclear forces that are not accessible by experiment alone.

ACKNOWLEDGMENTS

We thank Andre Walker-Loud and Thomas Luu for the collaboration during initial stages of this work, and Zohreh Davoudi and Raul Briceno for their comments on the manuscript. Calculations were performed using computational resources provided by the Extreme Science and Engineering Discovery Environment (XSEDE), which is supported by National Science Foundation Grant No. OCI-1053575, NERSC (supported by U.S. Department of Energy Grant No. DE-AC02-05CH11231), and by the USQCD Collaboration. This research used resources of the Oak Ridge Leadership Computing Facility at the Oak Ridge National Laboratory, which is supported by the Office of Science of the U.S. Department of Energy under Contract No. DE-AC05-00OR22725. Parts of the calculations used the CHROMA software suite [80]. S. R. B. was partially supported by NSF Continuing Grant

No. PHY1206498 and by the U.S. Department of Energy through Grant No. DE-SC001347. W. D. was supported in part by U.S. Department of Energy Early Career Research Award No. DE-SC0010495. K. O. was supported by the U.S. Department of Energy through Grant No. DE-FG02-04ER41302 and through Contract No. DE-AC05-06OR23177 under which JSA operates the Thomas Jefferson National Accelerator Facility. The work of A. P. was supported by Contract No. FIS2011-24154 from MEC (Spain) and FEDER. M. J. S. was supported in part by U.S. DOE Grant No. DE-FG02-00ER41132. This research was supported in part by the National Science Foundation under Grant No. NSF PHY11- 25915 and W. D. and M. J. S. acknowledge the Kavli Institute for Theoretical Physics for its hospitality during completion of this work.

[1] S. Borsanyi, S. Dürr, Z. Fodor, C. Hoelbling, S. Katz *et al.*, Science **347**, 1452 (2015).
[2] S. R. Beane, P. Bedaque, K. Orginos, and M. Savage, Phys. Rev. Lett. **97**, 012001 (2006).
[3] N. Ishii, S. Aoki, and T. Hatsuda, Phys. Rev. Lett. **99**, 022001 (2007).
[4] S. R. Beane, W. Detmold, H.-W. Lin, T. C. Luu, K. Orginos, M. J. Savage, A. Torok, and A. Walker-Loud (NPLQCD Collaboration), Phys. Rev. D **81**, 054505 (2010).
[5] S. R. Beane, W. Detmold, T. C. Luu, K. Orginos, A. Parreño, M. J. Savage, A. Torok, and A. Walker-Loud, Phys. Rev. D **80**, 074501 (2009).
[6] T. Yamazaki, Y. Kuramashi, and A. Ukawa (PACS-CS Collaboration), Phys. Rev. D **81**, 111504 (2010).
[7] S. R. Beane *et al.* (NPLQCD Collaboration), Phys. Rev. Lett. **106**, 162001 (2011).
[8] T. Inoue, N. Ishii, S. Aoki, T. Doi, T. Hatsuda, Y. Ikeda, K. Murano, H. Nemura, and K. Sasaki (HAL QCD), Prog. Theor. Phys. **124**, 591 (2010).
[9] S. R. Beane, W. Detmold, K. Orginos, and M. Savage, Prog. Part. Nucl. Phys. **66**, 1 (2011).
[10] T. Yamazaki, Y. Kuramashi, and A. Ukawa (PACS-CS Collaboration), Phys. Rev. D **84**, 054506 (2011).
[11] S. R. Beane, E. Chang, W. Detmold, H. W. Lin, T. C. Luu, K. Orginos, A. Parreño, M. J. Savage, A. Torok, and A. Walker-Loud (NPLQCD Collaboration), Phys. Rev. D **85**, 054511 (2012).
[12] K. Murano, N. Ishii, S. Aoki, and T. Hatsuda, Prog. Theor. Phys. **125**, 1225 (2011).
[13] T. Doi, S. Aoki, T. Hatsuda, Y. Ikeda, T. Inoue, N. Ishii, K. Murano, H. Nemura, and K. Sasaki (HAL QCD Collaboration), Prog. Theor. Phys. **127**, 723 (2012).
[14] S. R. Beane, E. Chang, S. D. Cohen, W. Detmold, H. W. Lin, T. C. Luu, K. Orginos, A. Parreño, M. J. Savage, and A. Walker-Loud, Phys. Rev. D **87**, 034506 (2013).
[15] T. Yamazaki, K.-i. Ishikawa, Y. Kuramashi, and A. Ukawa, Phys. Rev. D **86**, 074514 (2012).
[16] S. Aoki, T. Doi, T. Hatsuda, Y. Ikeda, T. Inoue, N. Ishii, K. Murano, H. Nemura, and K. Sasaki (HAL QCD Collaboration), Prog. Theor. Exp. Phys. **2012**, 01A105 (2012).
[17] S. R. Beane *et al.* (NPLQCD Collaboration), Phys. Rev. C **88**, 024003 (2013).
[18] N. Ishii (HAL QCD Collaboration), *Proc. Sci.*, CD12 (2013) 025.
[19] T. Yamazaki, K.-I. Ishikawa, Y. Kuramashi, and A. Ukawa, *Proc. Sci.*, LATTICE2013 (2014) 230 [arXiv:1310.5797].
[20] K. Murano, N. Ishii, S. Aoki, T. Doi, T. Hatsuda, Y. Ikeda, T. Inoue, H. Nemura, and K. Sasaki (HAL QCD Collaboration), Phys. Lett. B **735**, 19 (2014).
[21] T. Yamazaki, K.-i. Ishikawa, Y. Kuramashi, and A. Ukawa, Phys. Rev. D **92**, 014501 (2015).
[22] E. Berkowitz, T. Kurth, A. Nicholson, B. Joo, E. Rinaldi, M. Strother, P. M. Vranas, and A. Walker-Loud, arXiv:1508.00886.
[23] S. R. Beane, E. Chang, S. Cohen, W. Detmold, H. W. Lin, K. Orginos, A. Parreño, M. J. Savage, and B. C. Tiburzi, Phys. Rev. Lett. **113**, 252001 (2014).
[24] E. Chang, W. Detmold, K. Orginos, A. Parreno, M. J. Savage, B. C. Tiburzi, and S. R. Beane, arXiv:1506.05518 [Phys. Rev. D (to be published)].
[25] S. R. Beane, E. Chang, W. Detmold, K. Orginos, A. Parreño, M. J. Savage, and B. C. Tiburzi, Phys. Rev. Lett. **115**, 132001 (2015).
[26] S. R. Beane, E. Chang, S. D. Cohen, W. Detmold, H. W. Lin, T. C. Luu, K. Orginos, A. Parreño, M. J. Savage, and A. Walker-Loud, Phys. Rev. Lett. **109**, 172001 (2012).
[27] N. Barnea, L. Contessi, D. Gazit, F. Pederiva, and U. van Kolck, Phys. Rev. Lett. **114**, 052501 (2015).
[28] V. Baru, E. Epelbaum, A. A. Filin, and J. Gegelia, Phys. Rev. C **92**, 014001 (2015).
[29] S. Meinel (private communication).
[30] M. Lüscher and P. Weisz, Commun. Math. Phys. **97**, 59 (1985).
[31] B. Sheikholeslami and R. Wohlert, Nucl. Phys. **B259**, 572 (1985).
[32] C. Morningstar and M. J. Peardon, Phys. Rev. D **69**, 054501 (2004).
[33] R. Hoffmann, A. Hasenfratz, and S. Schaefer, *Proc. Sci.*, LAT2007 (2007) 104 [arXiv:0710.0471].
[34] R. G. Edwards, B. Joo, and H.-W. Lin, Phys. Rev. D **78**, 054501 (2008).
[35] Z. S. Brown, W. Detmold, S. Meinel, and K. Orginos, Phys. Rev. D **90**, 094507 (2014).
[36] M. A. Clark, B. Joo, A. D. Kennedy, and P. J. Silva, Phys. Rev. D **84**, 071502 (2011).
[37] M. A. Clark, R. Babich, K. Barros, R. Brower, and C. Rebbi, Comput. Phys. Commun. **181**, 1517 (2010).
[38] R. Babich, M. A. Clark, B. Joo, G. Shi, R. Brower, and S. Gottlieb, in *Proceedings of the International Conference for*

High Performance Computing, Networking, Storage and Analysis (SC11), Seattle, 2011 (Association for Computing Machinery, New York, 2011), p. 1517.
[39] W. Detmold and K. Orginos, Phys. Rev. D **87**, 114512 (2013).
[40] S. R. Beane, W. Detmold, T. C. Luu, K. Orginos, A. Parreño, M. J. Savage, A. Torok, and A. Walker-Loud, Phys. Rev. D **79**, 114502 (2009).
[41] M. G. Endres, D. B. Kaplan, J.-W. Lee, and A. N. Nicholson, Phys. Rev. Lett. **107**, 201601 (2011).
[42] W. Detmold and M. G. Endres, Phys. Rev. D **90**, 034503 (2014).
[43] J. L. Hodges and E. L. Lehman, Ann. Math. Stat. **34**, 598 (1963).
[44] S. R. Beane, W. Detmold, K. Orginos, and M. J. Savage, J. Phys. G **42**, 034022 (2015).
[45] E. E. Jenkins and A. V. Manohar, Phys. Lett. B **255**, 558 (1991).
[46] M. Gell-Mann, Phys. Rev. **125**, 1067 (1962).
[47] S. Okubo, Prog. Theor. Phys. **27**, 949 (1962).
[48] R. F. Dashen, E. E. Jenkins, and A. V. Manohar, Phys. Rev. D **51**, 3697 (1995).
[49] S. R. Beane, K. Orginos, and M. J. Savage, Phys. Lett. B **654**, 20 (2007).
[50] A. Walker-Loud *et al.*, Phys. Rev. D **79**, 054502 (2009).
[51] R. A. Briceño, Z. Davoudi, T. Luu, and M. J. Savage, Phys. Rev. D **88**, 114507 (2013).
[52] J. M. Blatt and L. C. Biedenharn, Phys. Rev. **86**, 399 (1952).
[53] M. Lüscher, Commun. Math. Phys. **105**, 153 (1986).
[54] M. Lüscher, Nucl. Phys. **B354**, 531 (1991).
[55] S. R. Beane, P. F. Bedaque, A. Parreño, and M. J. Savage, Phys. Lett. B **585**, 106 (2004).
[56] S. Bour, S. Koenig, D. Lee, H. W. Hammer, and U.-G. Meißner, Phys. Rev. D **84**, 091503 (2011).
[57] Z. Davoudi and M. J. Savage, Phys. Rev. D **84**, 114502 (2011).
[58] S. He, X. Feng, and C. Liu, J. High Energy Phys. 07 (2005) 011.
[59] R. A. Briceño and Z. Davoudi, Phys. Rev. D **88**, 094507 (2013).
[60] R. A. Briceño, Z. Davoudi, and T. C. Luu, Phys. Rev. D **88**, 034502 (2013).
[61] M. Rentmeester, http://nn-online.org (2005).
[62] E. Epelbaum, H.-W. Hammer, and U.-G. Meissner, Rev. Mod. Phys. **81**, 1773 (2009).
[63] R. Machleidt and D. R. Entem, Phys. Rep. **503**, 1 (2011).
[64] S. Binder *et al.*, arXiv:1505.07218.
[65] S. Weinberg, Phys. Lett. B **251**, 288 (1990).
[66] S. Weinberg, Nucl. Phys. **B363**, 3 (1991).
[67] C. Ordonez and U. van Kolck, Phys. Lett. B **291**, 459 (1992).
[68] D. B. Kaplan, M. J. Savage, and M. B. Wise, Phys. Lett. B **424**, 390 (1998).
[69] D. B. Kaplan, M. J. Savage, and M. B. Wise, Nucl. Phys. **B534**, 329 (1998).
[70] D. B. Kaplan, M. J. Savage, and M. B. Wise, Phys. Rev. C **59**, 617 (1999).
[71] S. R. Beane, P. F. Bedaque, M. J. Savage, and U. van Kolck, Nucl. Phys. **A700**, 377 (2002).
[72] J. Kirscher, Ph.D. thesis, George Washington University, 2011, http://inspirehep.net/record/1373970/files/arXiv:1506.00347.pdf.
[73] J. Kirscher, N. Barnea, D. Gazit, F. Pederiva, and U. van Kolck, Phys. Rev. C **92**, 054002 (2015).
[74] T. Mehen and I. W. Stewart, Nucl. Phys. **A665**, 164 (2000).
[75] S. Fleming, T. Mehen, and I. W. Stewart, Nucl. Phys. **A677**, 313 (2000).
[76] S. R. Beane, D. B. Kaplan, and A. Vuorinen, Phys. Rev. C **80**, 011001 (2009).
[77] E. Epelbaum, H. Krebs, and U. G. Meißner, Eur. Phys. J. A **51**, 53 (2015).
[78] H. P. Stapp, T. J. Ypsilantis, and N. Metropolis, Phys. Rev. **105**, 302 (1957).
[79] T. Yamazaki, arXiv:1511.09179.
[80] R. G. Edwards and B. Joo (SciDAC, LHPC, and UKQCD Collaborations), Nucl. Phys. B, Proc. Suppl. **140**, 832 (2005).